Estimation and Control of a Multi-Vehicle Testbed Using GPS Doppler Sensing

by

Nicholas A. Pohlman

Bachelor of Mechanical Engineering, University of Dayton, May 2000

Submitted to the Department of Aeronautics and Astronautics
in partial fulfillment of the requirements for the degree of

Master of Science in Aeronautics and Astronautics

at the

MASSACHUSETTS INSTITUTE OF TECHNOLOGY

September 2002

Author .....
Department of Aeronautics and Astronautics
September 1, 2002

Certified by .....
Jonathan P. How
Associate Professor
Thesis Supervisor

Accepted by .....
Edward M. Greitzer
Professor of Aeronautics and Astronautics
Chair, Committee on Graduate Students

Estimation and Control of a Multi-Vehicle Testbed Using GPS Doppler Sensing

by

Nicholas A. Pohlman

Submitted to the Department of Aeronautics and Astronautics
on September 1, 2002, in partial fulfillment of the
requirements for the degree of
Master of Science in Aeronautics and Astronautics

Abstract

This thesis presents estimation and control algorithms used to coordinate a multi-vehicle testbed. A total sensor package using the Global Positioning System as the primary sensor with secondary inertial sensors for when GPS is not available and a single point position fix measurement is designed. A new method of integrated velocity estimation is presented using only the Doppler measurements provided by the GPS NAVSTAR constellation. This shows significant improvement on previously used velocity integration methods by elminating unmodeled sensor biases. Furthermore, the algorithm includes the ability to calibrate inertial sensor biases in real-time, which are then used when observability to the constellation is blocked. The single point position fix is able to determine the initial position of the estimation or reset position estimation error drift. Methods are also presented for doing the low-level velocity and heading control of the test vehicle as well as nonlinear closed-loop path following control. Results of multiple estimation algorithms are presented showing that position accuracy with integrated velocity from a coupled GPS/INS/postion fix package is on the order of 10–30 cm over elapsed time of 2–3 minutes. While these errors are larger than CDGPS, the values are lower than typically available from absolute or differential Code phase, and this approach does not have the additional complexity of solving the CDGPS biases. Experiments also demonstrate the robustness and reliability of the path following algorithm. The designed testbed therefore has the necessary estimation and control capability to complete hardware-in-the-loop path following experiments.

Thesis Supervisor: Jonathan P. How
Title: Associate Professor

Acknowledgments

I would like to thank many people who have helped make this research work a reality. First, to my research advisor Professor Jonathan How, whose insight in both estimation and control techniques have helped solve many problems. I appreciate the effort and support to making the testbed work such that it can support future research.

I would also like to thank the many people at MIT who have made this experience educational and enjoyable - Chanwoo Park for initially introducing me to the GPS work and its applications; Many theoretical and social discussions were enjoyed with Arthur Richards, Philip Ferguson, Franz Busse, John Bellingham, Michael Tillerson, and Zachary Traina. I appreciate everyone's help in carrying equipment back and forth to the outdoor test area.

Lastly, I would like to thank my family for their continuous support. Without their initial push, I would not have enjoyed the academic experience as much as I have. Especially, I would like to thank my wife, Melaine. Through all of the technical detail problems during the research, she helped me keep focused and driven to complete this body of work - forever I am grateful.

Contents

1 Introduction **13**

1.1 Precise Estimation 13

1.2 Path Following Control 16

1.3 Hardware Selection 17

1.4 Outline 17

2 Measurements & State Estimation **19**

2.1 Measurement Concepts 19

2.1.1 GPS 19

2.1.2 Inertial Systems 28

2.1.3 Single Point Position Fix 29

2.2 The Extended Kalman Filter 33

2.2.1 Time Propagation 34

2.2.2 Measurement Update 36

2.3 Estimation Conclusions 42

3 Vehicle Control **43**

3.1 Speed Control 43

3.2 Heading Control 45

3.3 Position Control 46

3.3.1 Heading provided by plan 47

3.3.2 Proportional position control 48

3.3.3 Heading Autopilot with ground track control 50

3.4 Control Conclusions 53

4 Experimental Results **55**

4.1 Hardware 55

4.1.1 GPS Receivers 55

4.1.2 Base Station Computing 56

4.1.3 Transportation Equipment 57

4.1.4 Micro-Controller 58

4.1.5 Communication 59

4.1.6 Power 60

4.1.7 Hardware connections 60

4.2 Receiver Measurement Tests 61

4.3 Dynamic Testing of Velocity Integration 64

4.4 Bias Estimation Results 66

4.5 Control Results 74

4.5.1 Control of a Single Vehicle 74

4.5.2 Full Testbed Experiment 77

4.6 Experimental Conclusions 79

5 Conclusions **81**

5.1 New Estimation Method 81

5.2 Autonomous Testbed 81

5.3 Future Work 82

5.3.1 Estimation 82

5.3.2 Test Bed Improvements 82

A Fabrication and Software Interface **85**

A.1 Hardware Devices 85

A.2 Software Interface 86

List of Figures

2-1 Generic GPS receiver tracking loop block diagram [50] 21
2-2 Integer bias between receivers tracking the same transmitter signal . . 24
2-3 Laser position set-up for single point position fix 30
2-4 Rigid body motion of Ellis bicycle model 34
2-5 Cascaded filters indicated measurements and control inputs to each . 37

3-1 Speed closed-loop control block diagram 44
3-2 Speed closed-loop control response 44
3-3 Heading closed-loop control response 46
3-4 Ground vehicle closed-loop position control 47
3-5 Proportional control model 49
3-6 Autopilot ground track control model 50

4-1 Tamiya Mammoth Dump Truck with electronics payload 58
4-2 Hardware connections for individual truck components 61
4-3 DGPS Velocity Measurements of a Stationary Antenna 62
4-4 Velocity comparison of GPS WLS Doppler solution versus Pendulum speed 63
4-5 Integrated GPS velocity from differential Doppler measurements . . . 65
4-6 Close-up of start/end of figure 4-5 65
4-7 Position results of GPS and Coupled EKF - Run 33 67
4-8 Area around GPS signal loss and reacquisition 67
4-9 Close-up of area around single point position fix measurement 70
4-10 Area around start/finish position 70

4-11 Position results of GPS and Coupled EKF - Run 35 72
4-12 Position results of GPS and Coupled EKF - Run 37 72
4-13 Position results of GPS and Coupled EKF - Run 39 73
4-14 Multiple autonomous control runs 74
4-15 Final position of control experiments 76
4-16 Final position of control experiment with rotated reference frame . . 76
4-17 Control error of final position 77
4-18 Two trucks trading places while avoiding obstacles and collision with one another 78
4-19 Test of dynamic planning algorithm that adjusts plan while maneuvering 79

List of Tables

1.1 Function of individual measurement device in sensor package 14

2.1 Laser Positioning Error Expectations 32

4.1 Estimation Error Results (m) 73

A.1 Testbed hardware list for ground vehicle 85

A.2 Testbed hardware list for base station 86

A.3 Function keys to change display screen 86

A.4 Commands for “stargnd.exe” 87

Chapter 1

Introduction

This thesis demonstrates the development of a new sensor package and associated estimator incorporating GPS Doppler, inertial navigation sensors (INS) and a single point position fix. The estimation approach will be beneficial for robust high-precision state determination, such as racecar tracking. A new ground vehicle testbed has been created to demonstrate these estimation techniques. This thesis discusses the hardware selection for the testbed and presents the low-level control algorithms developed. The overall objective of the constructed testbed is for validation of hardware-in-the-loop advance path planning techniques [53, 55, 56]. Most planning applications are for Unmanned Air Vehicles or autonomous spacecraft maneuvers. The testbed presents a low-cost method for validation. The following subsections discuss each aspect of estimation and control in detail providing motivation and previous research work.

1.1 Precise Estimation

This research investigates the benefits of coupling three measurement systems:

1. GPS Doppler measurements;
2. Onboard vehicle speed and heading measurements; and
3. Single point position fix

Problem	Measurement Device		
	INS	GPS	Position Fix
Integration Drift			$\surd$
Initial Condition			$\surd$
Occlusions	$\surd$		
Sensor Biases		$\surd$	

Table 1.1: Function of individual measurement device in sensor package; $\surd$ denotes component solving problem

to produce a robust sensor package providing good estimation accuracy with continuous updates even with short losses to the precise GPS measurements. Integrating GPS velocity results provides the required position estimation accuracy if continuous visibility to signals is maintained. To compensate for signal occlusions due to the environment, an INS system is used to provide measurements when GPS is not available. The coupled filter can use simultaneous GPS/INS measurements to correct the inertial sensor bias errors such that better INS performance is achieved during GPS outages. However, since the filter is based on velocity measurements, there is no direct observation of the position state. The initial position is unknown and the position error drifts during the integration. The addition of a single-point position fix remedies both problems. Table 1.1 shows the components of the sensor package and contribution to the overall filter performance.

During the 1970's, the United States Air Force began to design a system for a worldwide, all weather navigation system for military maneuvers. After many years of testing and validation, the Global Positioning System (GPS) was officially activated for civilian use on April 27, 1995 [33]. Using a unique method for signal conditioning, the Navigation Satellite Timing and Ranging (NAVSTAR) constellation accurately provides the measurements necessary for determining precise state estimation.

The purpose of the Global Positioning System is to provide precise navigation solutions in a worldwide reference frame with an accuracy of 1–2 meters [50]. Many applications require more precise state knowledge but in much smaller localized regions. Indoor testbeds have been created using specialized local ranging devices [1, 52] such as pseudolites or electromagnetic techniques. The applications of this research

require larger operating regions than these approaches provide.

Research has shown hardware-in-the-loop precise relative estimation using differential GPS (DGPS) methods [41]. This allows expansion of the operating region for large scale experiments and added precision by eliminating common mode errors in the GPS measurements. But, using carrier-phase differential GPS (CDGPS) can maintain a robust estimation solution only in environments in which full NAVSTAR visibility is continuous [42]. Robustness can be added by using different aspects of the GPS signals, such as differential Code Phase, but the new measurements have significantly higher noise, which degrades the estimation accuracy.

To add robustness to state estimation, backup inertial sensors are included to provide measurements when the GPS signals are unavailable [30, 25]. Previous work has shown simple estimation methods using only INS causes significant state estimation error. Typical speed and turning rate integration methods over short time periods ($\approx$ 2 minutes) resulted in 50–100 m position error [10]. Two contributing sources cause the large estimation error. First, measurements from the sensors could simply be wrong due to improper assumptions, such as lateral accelerometers measuring gravity when the vehicle is pitched in a turn or wrong wheel radius adding a bias offset to axle encoders. The second significant error source is due to the inertial measurements determining states in localized vehicle reference frame. Any error associating the inertial measurement to an external reference frame is unobservable with a stand-alone INS system. Other research uses complementary measurement methods to couple the absolute reference frame measurements (GPS) to those from individual vehicles (INS) thereby reducing overall estimation error [24, 27]. The current research uses similar coupling methods, however the primary GPS measurement is from Doppler rather than the carrier-phase eliminating solution delay to solve for the CDGPS integer biases.

Many applications may benefit from this robust and precise estimation method. For example, racecar drivers are focused on completing a single lap in the shortest possible time. GPS receivers have shown the capability to solve rapid solutions even in such highly dynamic environments [21]. Accurate tracking of vehicle path enables

layover comparisons of vehicle performance [16]. By comparing similar instances, vehicle response with respect to input control could be used to compare driving line performance to help train new drivers [15]. Gross errors produced by inexperienced drivers are easily observable with simple sensors. However with precise estimates, enhancements in professional driver performance can be observed therefore offering suggestions for improvement. Additional applications to systems requiring precise state estimation for path control are discussed in the next section.

1.2 Path Following Control

The resulting estimator is used to perform path following closed-loop control. Given the desired state information for steps along the path, the methods presented in this thesis use appropriate controllers to move the vehicle along the path. A nested-loop design is implemented such that low-level controllers complete feedback control on state elements for speed and heading. Outer-loop designs are identified to complete closed-loop position control of individual vehicles. Other work suggests leader/follower fleet path control algorithms such that each vehicle within the fleet was required to continuously follow a manually controlled leader [18]. Closed-loop control in this research can follow a general path provided by any planning algorithm. This design enables rapid changes in vehicles or path planning algorithms to validate real-time receding horizon control.

The motivation for the control development is to complete testbed autonomous control maneuvers regardless of the method for path planning. Other applications include precision farming [4], autonomous aircraft landing [12], and Unmanned Air Vehicle maneuvering [45]. In particular, the testbed control can validate high-level control algorithms. Such algorithms have been developed for optimization of vehicle performance [17] and UAV fleet coordination.

1.3 Hardware Selection

This thesis identifies the components selected for fabrication of the multi-vehicle testbed. Similar testbeds have been developed in the past to test estimation and fleet coordination experiments. For the three-dimensional testbed using blimps [1], experiments were limited to indoor testing facilities, eliminating the possibility of using actual GPS satellite measurements. An outdoor ground testbed using real GPS equipment was constructed [44], however significant payload weight overloaded the vehicle suspension severely altering the test vehicle dynamic capability. Experimental results were obtained, but reliability of vehicle performance was not acceptable. In this research, a more robust transportation device was selected allowing all of the necessary payload for coordination control experiments to be carried without degrading the vehicle performance. Payload components necessary for sensor measurements, remote control and communication are identified.

1.4 Outline

The following chapters indicate the design and algorithms used to meet the desired objectives of the multi-vehicle testbed. Chapter 2 derives the extended Kalman filter used to produce the reliable and robust estimation algorithm using all available sensors. Control of all aspects of the vehicle, low-level speed and heading as well as path following algorithms, are presented in Chapter 3. The results of many experiments of both the estimation and control methods are given in Chapter 4. Finally, Chapter 5 concludes the research objectives achieved in the design and operation of the multi-vehicle testbed and presents future work that can help improve aspects of the new research testbed.

Chapter 2

Measurements & State Estimation

This chapter designs the extended Kalman filter used for the vehicle state estimation. Before formulating the specific Kalman filter equations, aspects of the measurement and process model are first introduced.

2.1 Measurement Concepts

This section reviews the construction of GPS signals and presents previous research showing how the signals have be used in similar estimation and control applications. Additionally, the design of the inertial sensors as well as the single position measurement system is introduced. Problems of individual systems are identified and explanations given for how the coupled GPS/INS estimator overcomes these shortcomings.

2.1.1 GPS

The original intent of the Global Positioning System was to create a robust navigation tool that could be used to find an absolute position in the worldwide reference frame [33]. Determining position with GPS is done by ranging to separate locations. Consider a range measurement ρ between a fixed transmitter t and user u with position vectors being measured from the origin of a coordinate frame, $\boldsymbol{\rho}^t$ and $\boldsymbol{\rho}_u$,

respectively

$$\rho \;=\; \|\boldsymbol{\rho}^t - \boldsymbol{\rho}_u\| \tag{2.1}$$

If the transmitter locations are known, only three measurements are required for a position solution. This section explains how GPS signals are formulated to provide range measurements and transmitter locations thus making it possible to estimate position and/or velocity for any user.

Signal Construction

The GPS signal is a high-frequency, low-power electromagnetic waveform that is being transmitted by the 24 NAVSTAR satellites simultaneously. A standard, inexpensive GPS receiver tracks the repeating Clear/Acquisition Code (C/A-Code), frequency 1.023MHz, being transmitted at the nominal carrier frequency of 1575.42MHz, also known as the L1 band. Signals are also being transmitted for the Precision Code (P-Code) on both L1 and the L2 band, which is at 1227.60MHz. The P-Code has been reserved for military use only, however the C/A-Code and its L1 carrier have proven to be useful for precise relative measurements [33, 34].

The C/A-Code is generated by a pseudorandom number (PRN) digital Code chosen from a select number of "Gold Codes" described in Ref. [48]. The 32 particular Codes were selected for GPS use because they have good auto-correlation properties and minimal cross-correlation, both of which are necessary for tracking and locking onto the GPS signal. The PRN Code is then combined with the satellite data message and the L1 carrier signal to be transmitted. Since each satellite has a unique PRN Code to transmit data, all signals can operate at the same frequency without interfering with one another.

In order to track the signal, the GPS receiver must be able to raise the transmitted signal out of the thermal noise floor at the L1 frequency. This is accomplished by using the tracking loop diagram shown in figure 2-1 from Ref. [50]. As shown at the left portion of the tracking loop, replica carrier signal waveforms are generated

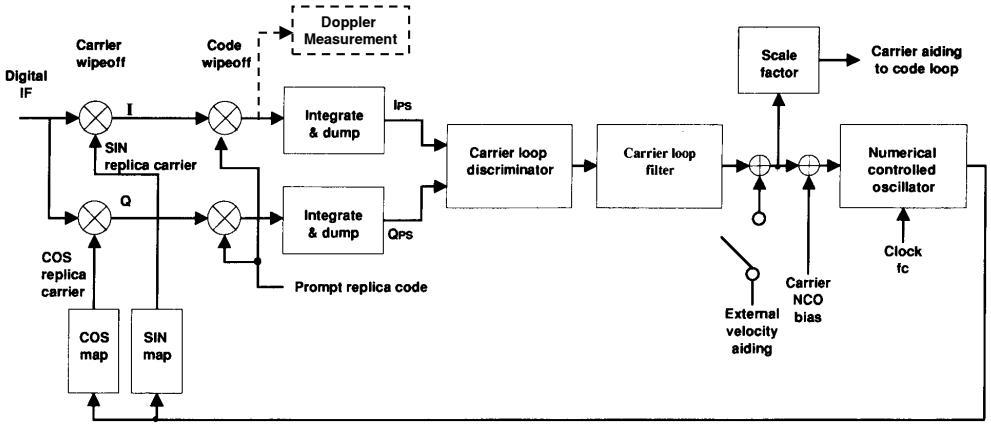

Figure 2-1: Generic GPS receiver tracking loop block diagram [50]

from the onboard oscillator, which then demodulate the input RF signal thereby isolating the PRN Code. Given the specified 32 PRN codes [35], GPS receivers can replicate the C/A-Code for all transmitting satellites. The receiver quickly slews the current PRN replica across the received signal. Since the cross-correlation of the Gold Codes is very minimal, and the auto-correlation very high, it is easily observed when the two are perfectly correlated. When the peak correlation between signal and replica is found, the receiver can then close the loop to maintain tracking of the C/A-Code. The real-time frequency control to maintain tracking lock on the PRN is the controllable input parameter, more often referred to as Doppler because of the frequency shifting. At a minimum, a GPS receiver reports the replicated Code Phase for all tracked signals as measured on GPS time. Receivers with more advanced communication also provide the carrier phase cycles measured from the beginning of signal acquisition and the Doppler values used in the correlator closed-loop control. It is this Doppler measurement from the GPS receiver that provides very precise velocity measurements for the new estimation method.

Range Measurements

This section discusses the principles for GPS range measurement and discusses why that they are not suitable for our application. The distance between a receiver and the i^{th} transmitter is calculated by determining the transmission time of the GPS

signal, commonly referred to as pseudorange (pr), with the simple model [34]

$$\begin{aligned} pr^i &= c(\hat{t}_k - t_{\text{satellite transmission}}) \\ &= \|\boldsymbol{\rho}^i - \boldsymbol{\rho}_u\| + c\tau_0 \end{aligned} \tag{2.2}$$

where c is the speed of light; $\hat{t}_k$, the receivers current estimate of GPS time; $t_{\text{sat. trans.}}$ is the time tag when the signal left the satellite. For equation 2.2, the range is from equation 2.1 and τ_0 is the error in the receivers estimate of GPS time. The outgoing satellite signal is synchronized to a standardized NAVSTAR system time determined from very stable onboard atomic clocks. Measuring the elapsed time is a function of distance as well as the accuracy of estimated time onboard the receiver.

Because the waveforms are continuously repeating, the actual measurements provided by the receiver are the accumulated phases ϕ of the signal. The phase quantity plus the integer number of wavelengths is the actual range between transmitter and receiver. If the integer β_0 is separated from the total range and included in the measurement model, the phase equation, including error sources, for both the Code and carrier phase from the i^{th} GPS satellite is expressed as [34]

$$\begin{aligned} \phi^i &= \frac{1}{\lambda}\sqrt{(x^i - x)^2 + (y^i - y)^2 + (z^i - z)^2}/ + \\ &\quad \frac{c}{\lambda}(\tau^i - \tau_R) + \beta_0^i + \epsilon_{\text{atmospheric}} + \nu \end{aligned} \tag{2.3}$$

where:

x^i, y^i, z^i = Position coordinates of i^{th} GPS satellite in an ECEF reference frame

x, y, z = Position coordinates of the receiver in an ECEF reference frame

c = Speed of light

τ^i = Clock bias of the i^{th} GPS satellite to actual GPS time

τ_R = Clock bias of the receiver to actual GPS time

β_0 = Integer number of wavelengths between GPS satellite and user at start-up; Sign is negative

ϵ = Pseudorange transmission delays due to atmospheric disturbances

λ = Wavelength of tracked signal; 300 km for Code waveform and 19 cm for carrier

ν = Noise on the carrier phase measurement

To maintain the integrity of the system, the satellite locations (x^i, y^i, z^i) and individual clock drifts τ^i are precisely monitored and updated by the GPS control center stationed in Colorado Springs and other tracking stations in the global network. To solve for the three elements of the absolute navigation solution as well as receiver clock bias, phase measurements are required from four unique satellites [33].

The accuracy of this absolute position estimation is approximately 1–2 meters when Selective Availability (SA) if off [50]. (SA was the degradation of GPS time purposely added in order to reduce position accuracy; It was removed from the GPS signals May 1, 2000) [49]. The inaccuracy of the absolute estimate can be traced back to the measurements used to compute the navigation solution. First, errors included in the measurements, such as satellite clock bias and atmospheric delays, are not observable and therefore cannot be eliminated in the estimation filter. Second, all absolute solutions must use the Code phase measurements rather than the carrier phase, due to the integer bias term β_0^i in equation 2.3. Because Code phase has a much longer wavelength than carrier phase, fewer combinations of the β_0^i must be searched to determine the integer wavelengths between the user and transmitting satellite. With the short wavelength of the carrier wave, the carrier bias is impossible to solve in an absolute sense. The Code phase measurement noise is based on the ability to track the 1023 binary chips in the PRN Code. The wavelength of a single chip is ≈ 300 m thus with 0.1% tracking accuracy, there is ≈ 30 cm of noise on each measurement, resulting in the limited navigation accuracy. Conversely, if the carrier phase is tracked with 10% phase accuracy the measurement noise will be ≈ 2 cm making it a better tool for precise estimation.

Because of the short wavelength, carrier phase absolute estimation is nearly impossible, thus methods have been developed to use the precise carrier phase for relative estimation. Carrier-Phase Differential GPS (CDGPS) is formed by taking the single

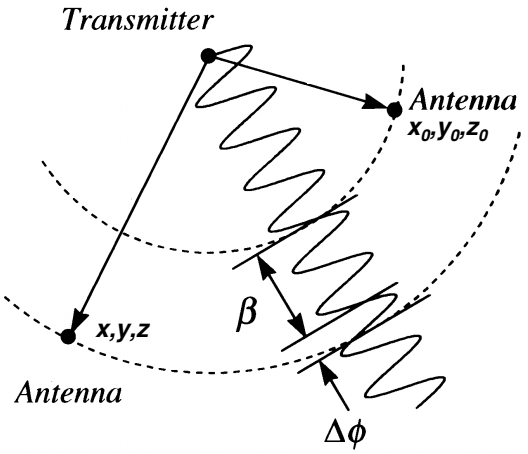

Figure 2-2: Integer bias between receivers tracking the same transmitter signal

difference between common satellite phase measurements of two receivers [34]. Differential GPS attempts to eliminate linear common mode errors, such as satellite clock drift and atmospheric delay, from the measurement equation. The differential phase measurement is a function of relative position states and clock biases between two receivers

$$\Delta\phi^i = \frac{1}{\lambda}\sqrt{\Delta x^2 + \Delta y^2 + \Delta z^2} + \frac{c}{\lambda}\Delta\tau_R + \beta^i + \nu \tag{2.4}$$

where $(\Delta x, \Delta y, \Delta z)$ is the relative position vector of the antennas and $\Delta\tau_R$ is the relative clock bias between the receivers estimate of time. Note that in equation 2.4, there is a bias term, β^i similar to β_0^i in equation 2.3, representing the integer ambiguity present in the relative range measurement of the carrier frequency wave, shown in figure 2-2. The single difference equation is valid for Code phase measurements as well, thereby improving upon the absolute navigation accuracy, however the large phase measurement noise is still present.

The primary difficulty of CDGPS is in that the bias must be re-initialized each time a new measurement is acquired, even after only a brief loss of tracking. Previous research has shown many ways to estimate the measurement integer ambiguity [14]. If the relative position is known exactly, the biases can be determined immediately.

But, any error introduced by the initial guess causes a slow drift of the position estimation error due to the motion of the GPS constellation. Furthermore, once displacement from the origin occurs, exact bias estimates of newly acquired signals or signals blocked for any period of time cannot be solved. Initializing the carrier phase biases using the initial position method is limited to very short-term applications that maintain continuous sky visibility. Another method to find the ambiguity precisely is to keep all antennas stationary and record the raw tracking data. As the satellites continue on their orbit, the angle of the line-of-sights will change making the integer values observable. The bias is then solved by finding the integer combination that best matches all of the measurements. However, a time delay of 20–40 minutes is often required in order to obtain a sufficient rotation of the NAVSTAR satellites. If a fixed baseline distance between antennas is maintained, the ambiguity can be determined by rotating the antennas to switch locations of the base and remote receivers [5]. Otherwise if the fixed baseline distance is known, a fast integer combination search can be conducted [6]. The benefit of fixed baseline CDGPS estimation is the ability to determine the rigid body attitude in the reference frame. Given the CDGPS solution in the GPS frame, Wahba's problem [11] can be solved to determine the body frame rotation.

Since most dynamic applications required faster start-up, instantaneous on-the-fly (OTF) procedures have also been developed. Two means for OTF initialization are augmenting the GPS system with a local ranging device or having the receiver track the L2 GPS frequency. Note that both methods typically require a significant increase in equipment costs. Pseudolites that generate exact replicas of the GPS Code can be mounted around the area of use, thereby giving local range measurements without having to add any additional sensing hardware [2, 4, 12]. Rapid changes in the local line-of-sight to the nearby pseudolite can be used to quickly determine the integer biases. Because the pseudolite signal does not contain the standard GPS data messages, the receiver tracking algorithm must be modified to create accurate local ranging measurements. Furthermore, the signal power of the pseudolite must be tuned in order not to inhibit the signals of the GPS satellites from being observable

to the receiver RF [2]. Also, far field assumptions for parallel lines-of-sight are no longer valid and adjustments must be made for the nonlinear effects of the local range measurements for short path initialization [3].

Another option is to use a dual frequency receiver that tracks the L2 band at 1227.60MHz as well as L1. The *widelaning* technique produces Real-Time Kinematic (RTK) relative position solutions by measuring the phase of the beat frequency (347.82MHz) of the two bands. This new measurement has a wavelength of ≈ 86 cm, which significantly decreases the required integer search space, thus the ambiguity can be solved almost instantaneously [13]. While this method proves to be quick and robust, it typically requires a significantly more expensive GPS receiver.

Research has improved methods for integer bias acquisition of L1 band carrier, and once determined, the measurement can provide useful and accurate range information to the estimator. Yet, it has still proven to be difficult when GPS signals are not continuously tracked [42]. Differential Code phase does not have the delayed integer bias acquisition problem, however the pseudorange accuracy is insufficient due to the longer wavelength. Therefore, other available measurements from the Global Position System were considered for the estimator development.

Range Rate Measurements

Rather than focus on new methods for solving integer ambiguity in environments without continuous visibility, this research explores ways to use the Doppler information to obtain a precise estimate of the velocity of the vehicle. Using the Doppler measurements enables precise estimation immediately after signal lock, thereby eliminating the delay of integer ambiguity computation. Future sections present methods to create continuous state estimation even during signal occlusion by incorporating backup inertial sensors.

The phase equation 2.3 can be differentiated to form a phase rate measurement

model to the i^{th} GPS satellite [41]

$$\dot{\phi}^i = \frac{1}{\lambda}\begin{bmatrix} (\dot{x}^i - \dot{x}) \\ (\dot{y}^i - \dot{y}) \\ (\dot{z}^i - \dot{z}) \end{bmatrix}^T \begin{bmatrix} \frac{(x^i-x)}{\sqrt{(x^i-x)^2+(y^i-y)^2+(z^i-z)^2}} \\ \frac{(y^i-y)}{\sqrt{(x^i-x)^2+(y^i-y)^2+(z^i-z)^2}} \\ \frac{(z^i-z)}{\sqrt{(x^i-x)^2+(y^i-y)^2+(z^i-z)^2}} \end{bmatrix} + \frac{c}{\lambda}(\dot{\tau}^S - \dot{\tau}_R) + \dot{\epsilon} + \dot{\nu} \tag{2.5}$$

Equation 2.5 represents the projection (scalar product) of the relative velocity vector between receiver and transmitter (transposed vector on left) onto the vector connecting the user to the satellite, more commonly referred to as the line-of-sight (**los**). The remaining variables, other than position of satellite and user, are the rates of the terms in equation 2.3. The line-of-sight is a unit vector pointing from the absolute position of the user receiver to the absolute position of the tracked satellite. Since the absolute user position is typically available from the pseudorange solution and the ephemeris information of each satellite is transmitted in the GPS data message, the **los** can easily be formed. Errors of the absolute position solution contribute negligible error to the **los** calculation. The significant difference that must be noted between equations 2.3 and 2.5 is the elimination of the bias term β^i. Without the delay to determine the bias term, estimation can begin using Doppler measurements immediately after Code phase lock.

In order to reduce common mode errors, differential Doppler GPS creates the single difference between two phase rate measurements, user j and base station b, to the i^{th} satellite forming

$$\Delta\dot{\phi}^i_j = \mathbf{los}^i_j \bullet \dot{\mathbf{x}}_{j,\mathrm{GPS}} - \mathbf{los}^i_b \bullet \dot{\mathbf{x}}_{b,\mathrm{GPS}} + \Delta\dot{\tau} + \dot{\nu} \tag{2.6}$$

where $\Delta\dot{\tau}$ is the relative clock drift between receivers and $\dot{\mathbf{x}}$ is the vector of velocity components. As indicated previously, the measurement itself is provided from the instantaneous state in the correlator tracking loop filter. Since typical noise values on these measurements are $0.5 - 1.0$ mm/s and primarily white (see discussion in Chap-

ter 4) a properly formulated filter will produce highly accurate velocity estimates with small levels of noise that are primarily white. Given the initial location, the velocity can be integrated for position estimation. A random walk for the position estimation error is generated due to the near-white noise embedded in the velocity estimate. Experiments have shown that, even with the position error drift, estimation using only Doppler measurements provides immediate short-term full state estimation with greater accuracy achievable than from differential Code phase estimation. Assuming Code phase accuracy of $1-2$ meters and Doppler position estimation drift ≈ 2 mm/s, the Doppler solution will have better performance for up to 10 minutes before reaching differential Code phase accuracy.

2.1.2 Inertial Systems

In order to add continuous measurement capability to the system, back-up sensors can be included on the test vehicle to provide information when the GPS Doppler measurements are unavailable [30, 28]. Typically, in aerospace applications, these devices have a higher fidelity resulting in significant cost. Research has shown that even low cost sensors can be incorporated into a GPS/INS system to achieve accurate estimation results [25]. This section introduces different inertial measurement sensors and potential errors that contribute to estimation inaccuracy. By using simultaneous measurements from separate devices, estimates of the sensor error can be determined thereby improving the accuracy of the overall system [27].

A wide range of potential sensors such as wheel speed encoders, lateral accelerometers, and turning rate gyros could be used to measure variables on the ground-vehicle. In each of the example sensors, the measured quantity is a function of the rates of position or heading. As stated, the motivation for this research is primarily to create precise position estimation. Previous research has shown that simple integration of these rate measurements over time results in significant position estimation error (50–100m) [10]. The current method uses the precise GPS velocity estimate to determine INS sensor errors such that inertial measurements can be improved for operation during short-term GPS signal losses.

The estimate from GPS sensing solves the relative velocity vector of the user. Therefore, a similar result of measuring speed and heading was desired from the set of INS sensors. The sensor package design was augmented with a wheel axle encoder and a magnetic compass. Assumptions were made about sources contributing to measurement error of the speed and heading. For example, the wheel speed encoder can only be attached to one drive shaft and is affected by tire slip and additional rotation due to the tire having a lateral offset from the center of gravity. Similarly, the compass can be effected by magnetics in the ground vehicle drive motor. Rather than assuming complex measurement models, all errors in the inertial sensors are modeled as additive bias terms. In the filter, the bias states are modeled as integrators driven by zero mean white noise. An estimation scheme that appropriately couples the two measurement capabilities of GPS and inertial sensor is able to determine the steady-state biases in real-time producing a continuous, robust capability while still providing accurate results.

2.1.3 Single Point Position Fix

Accuracy of velocity integration techniques is a function of the precision of the initial position supplied to the system as well as the error drift caused by velocity noise. Applications where similar paths must be compared (i.e. racecar performance) provide a natural position update at the start/finish line. A limitation is produced, however in that the lateral position of the vehicle cannot be directly determined by breaking a single line. A technique was devised to use two non-parallel laser beams to produce a single point position measurement that can start the integration method or possibly allow a reset of a slowly diverging estimator.

The set-up consists of two transmitting lasers, in our case pen lights, with optical receivers across the path the vehicle traverses. Figure 2-3 shows a schematic indicating the geometric set-up used to determine a single position. The transmitter and receiver locations are denoted by $\mathbf{T}$ and $\mathbf{R}$, respectively. Each time the vehicle breaks a laser beam, the velocity state information $(\mathbf{V_1}, \mathbf{V_2})$ from the estimator is stored as well as the elapsed time between beams (ΔT). If a linear change of velocity is assumed

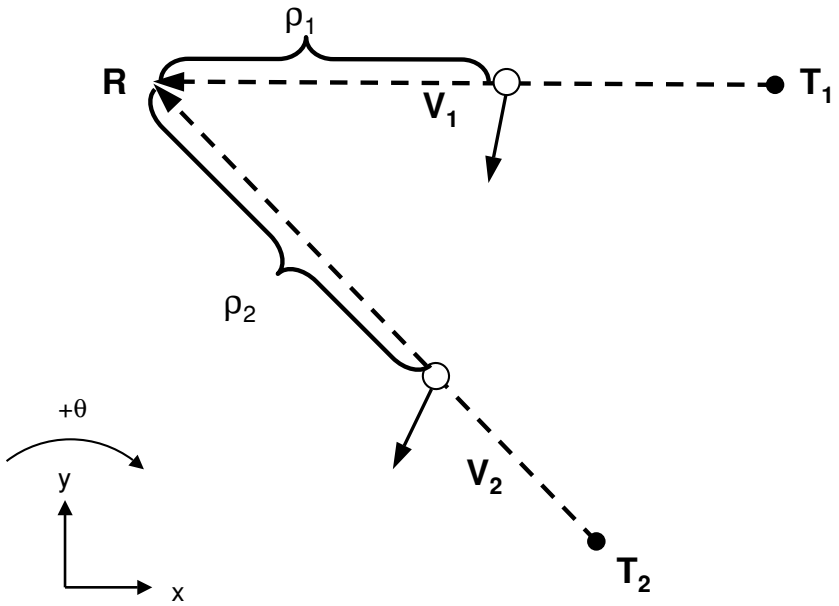

Figure 2-3: Laser position set-up for single point position fix

between the beams, an analytical function can be written for the velocity vector while traveling through the beams

$$\mathbf{V}(t) = \frac{(\mathbf{V_2} - \mathbf{V_1})}{\Delta T} t + \mathbf{V_1} \tag{2.7}$$

where t is the elapsed time between breaking the two laser beams. When equation 2.7 is integrated from 0 to ΔT to solve for the traveled path, a constant of integration is introduced

$$\mathbf{S}(t) = \int \mathbf{V}(t)\, \mathrm{d}t \tag{2.8}$$

$$= \frac{(\mathbf{V_2} - \mathbf{V_1})}{2\Delta T} t^2 + \mathbf{V_1} t + \mathbf{C} \tag{2.9}$$

The vector constant $\mathbf{C}$ is the two-dimensional vehicle position when the first laser is broken and located somewhere along the vector connecting the transmitter and receiver. The value of ρ_1 is the percentage along the vector $\mathbf{T_1} - \mathbf{R}$ that the vehicle breaks the beam, hence the initial condition can be produced and substituted into

equation 2.9

$$\begin{aligned} \mathbf{S}(0) &= \rho_1(\mathbf{T_1} - \mathbf{R}) + \mathbf{R} && (2.10) \\ \mathbf{S}(t) &= \frac{(\mathbf{V_2} - \mathbf{V_1})}{2\Delta T} t^2 + \mathbf{V_1} t + \rho_1(\mathbf{T_1} - \mathbf{R}) + \mathbf{R} && (2.11) \end{aligned}$$

To solve for the unknown parameter ρ_1, the terminal condition upon hitting the second beam after an elapsed time of ΔT must be included

$$\begin{aligned} \mathbf{S}(\Delta T) &= \rho_2(\mathbf{T_2} - \mathbf{R}) + \mathbf{R} \\ &= \frac{(\mathbf{V_2} + \mathbf{V_1})}{2} \Delta T + \rho_1(\mathbf{T_1} - \mathbf{R}) + \mathbf{R} && (2.12) \end{aligned}$$

The resulting vector equation has two unknown parameters, ρ_1 and ρ_2. If the receiver locations are set at the origin ($\mathbf{R} = (0, 0)$) and one beam is aligned horizontal to the reference frame ($\mathbf{T_1} = (T_{1,x}, 0)$) as shown in figure 2-3, the solution for ρ_2 collapses to

$$\rho_2 = \frac{V_{2,y} + V_{1,y}}{2T_{2,y}} \Delta T \quad (2.13)$$

which can then be substituted into the final position constraint in equation 2.12 to determine the positions

$$\begin{bmatrix} x \\ y \end{bmatrix} = \frac{V_{2,y} + V_{1,y}}{2T_{2,y}} \Delta T(\mathbf{T_2}) \quad (2.14)$$

If the location of $\mathbf{T_2}$ is created by setting the angle between beams, equation 2.14 can be rewritten as

$$\begin{aligned} x &= \frac{V_{2,y} + V_{1,y}}{2 \tan \theta_{T_2}} \Delta T && (2.15) \\ y &= \frac{V_{2,y} + V_{1,y}}{2} \Delta T \end{aligned}$$

where θ_{T_2} is the angle of separation from $\mathbf{T_1}$ to $\mathbf{T_2}$. By fixing the laser set-up to the

Table 2.1: Laser Positioning Error Expectations

Variable	Nominal	Absolute Error	% Error
$V_{1,y}$	1.2 m/s	0.002 m/s	
$V_{2,y}$	1.1 m/s	0.002 m/s	
$\frac{1}{2}(V_{1,y} + V_{2,y})$	1.15 m/s	0.004 m/s	0.35%
ΔT	1.86 sec	0.01 sec	0.54 %
$\tan\theta_{T_2}$	1.428	0.027	1.76%
	$(\theta_{T_2} = 55°)$	$(\Delta\theta_{T_2} = 0.5°)$	
Total % Error			2.55%

reference frame, the precision of this position update is a function of the accuracy of the velocity estimate at the time of breaking the beam, the accuracy to which ΔT can be measured and the angle θ_{T_2} between the beam vectors. If the angle of separation is small ($< 35°$), the lateral position along the beam vector results in a significantly large position measurement error. However, span angles that are too large introduce error in the linear velocity change assumption. Table 2.1 indicates individual variable contributions from equation 2.15 to the position measurement error expected from a typical set-up. The Total % Error can be multiplied by the distance from the receivers that a beam is broken to determine the position accuracy. For cases where the path is less than 1.2 meters away from $\mathbf{R}$, the position error is approximately 3 cm. This expected error can be included in the measurement noise model for the position update so that the filter does not assume a perfect measurement.

Note, the best position measurement accuracy is achieved closest to $\mathbf{R}$, where the two laser beams meet. If a receiver is created for each transmitter, the lines connecting $\mathbf{T_1}$-$\mathbf{R}$ and $\mathbf{T_2}$-$\mathbf{R}$ can be extended to the left such that an $\times$ is formed by the laser lines. This enables the area around the intersection to provide greatest position measurement accuracy. The error analysis verifies the expectation of θ_{T_2} to dominate component error contribution to the total error percentage. For improvement of position accuracy, work should focus on methods to improve the knowledge of θ_{T_2}.

2.2 The Extended Kalman Filter

For linear systems, the Kalman Filter produces the optimal recursive filter for full-state estimation [37, 36]. Updates to the state estimate are based on measurements, which often may not provide full state observability, as well as an expected state model. Given a model of the nonlinear vehicle dynamics, expected measurement values can be compared with actual sensor feedback providing a recursive estimate on the full state. An extended Kalman Filter (EKF) is required when propagation and measurement models have nonlinear representation. The models are then linearized when calculating parameters for the Kalman gain and covariance propagation.

The state vector of the designed estimator includes components for position, heading, and velocity in a two-dimensional frame relative to a base station reference

$$\mathbf{x} = \begin{bmatrix} N \\ E \\ \theta \\ \dot{N} \\ \dot{E} \\ \boldsymbol{\beta} \end{bmatrix} \tag{2.16}$$

The first two elements, (N, E), indicated the north and east positions respectively (with $(\dot{N}, \dot{E})$ representing the rates); θ is the current heading of the rigid body; The $\boldsymbol{\beta}$ term indicates those parts of the state vector necessary for measurement model memory, such as previous positions, sensor biases or GPS parameters. Future computations will require only the velocity elements of the state vector, therefore the velocity vector $\mathbf{V}$ is defined

$$\mathbf{V} = \begin{bmatrix} \dot{N} \\ \dot{E} \end{bmatrix} \tag{2.17}$$

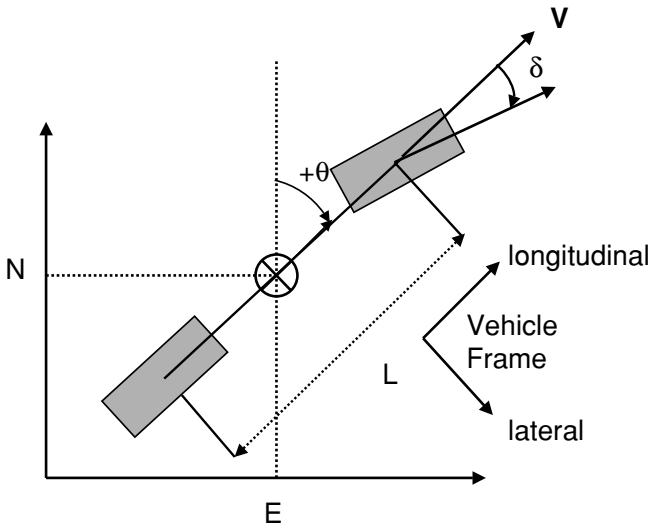

Figure 2-4: Rigid body motion of Ellis bicycle model with identified parameters

2.2.1 Time Propagation

Using a dynamics model, each element of the state can be propagated with a nonlinear function, $\mathbf{f}$, from the previous time step $(k-1)$ to the *a priori* estimate at the current time (k) using the previous state $\mathbf{x}_{k-1}$ and inputs to the system $\mathbf{u}_k$

$$\hat{\mathbf{x}}_k^- = \mathbf{f}(\hat{\mathbf{x}}_{k-1}, \mathbf{u}_k) \tag{2.18}$$

For rigid body motion of the test vehicle dynamics, the Ellis bicycle model [40] shown in Figure 2-4 was used for the land vehicle with no modeled side-slip. Since our initial application would only be operating at relatively slow speeds, this assumption does not introduce significant errors. Individual components of the velocity were created by multiplying the speed by the appropriate trigonometric function of heading

$$\dot{N}_{k+1} = (\|\mathbf{V}\| + \Delta u_v)\cos\theta \tag{2.19}$$

$$\dot{E}_{k+1} = (\|\mathbf{V}\| + \Delta u_v)\sin\theta \tag{2.20}$$

where Δu_v is the input parameter for the requested change in longitudinal speed. The value of θ is zero when aligned with the north vector and increases to $\pi/2$ when aligned directly east creating a North-East-Down reference frame.

The rate of change of the vehicle heading was modeled by

$$\dot{\theta}_k = \frac{\|\mathbf{V}\|}{L} \tan \delta \tag{2.21}$$

where L is the wheel base length of the vehicle and δ is the turning angle of the front wheels with respect to the vehicle frame, a controllable input.

In order to interpret position information from primarily velocity measurements, a first-order Forward Euler integration scheme was used

$$N_{k+1} = N_k + \dot{N}_k \Delta T \tag{2.22}$$

$$E_{k+1} = E_k + \dot{E}_k \Delta T \tag{2.23}$$

where ΔT is the change in discrete time between updates. The covariance matrix P, an indicator of the reliability of the particular state estimate, is propagated to the *a priori* value at the current time P_k^- from a linearized calculation

$$P_k^- = A_k P_{k-1} A_k^T + Q_{k-1} \tag{2.24}$$

where P_{k-1} is the covariance from the previous time step and Q_{k-1} is the assumed process noise effecting the state. The matrix A_k is the linear element of the Taylor series expansion of the state propagation equations about the current estimate of the state, $\mathbf{x}_k$

$$A_k = \left[\frac{\partial \mathbf{f}(\mathbf{x})}{\partial \mathbf{x}} \right]_{\hat{\mathbf{x}}_k} \tag{2.25}$$

The estimator begins with an initial position guess that typically is started from the origin, a surveyed location, or with an erroneous guess to be followed immediately by a position measurement update. Given the testbed vehicle dynamics model, estimates can then be made of the expected measurements from the sensor package and a state update from measurements can be produced.

2.2.2 Measurement Update

The remaining step of the Kalman filter is to incorporate the sensor measurements into the current estimate. The set of mathematical equations, $\mathbf{h}$, are a function of state vector elements that create expected sensor measurements

$$\hat{\mathbf{z}}_k = \mathbf{h}(\mathbf{x}_k^-) \tag{2.26}$$

where $\hat{\mathbf{z}}_k$ is the vector of measurement estimates and $\mathbf{x}_k^-$ is the *a priori* estimate from the time update step. Assumptions regarding state element contributions and error sources have been defined and the math models for each of the measurements available from the new GPS/INS sensor package are explained in further detail in future sections.

To create the linear measurement contribution to the Kalman gain K_k, the vector $\mathbf{h}$ is linearized via the Taylor series expansion to form H_k

$$H_k = \left[\frac{\partial \mathbf{h}(\mathbf{x})}{\partial \mathbf{x}}\right]_{\mathbf{x}_k^-} \tag{2.27}$$

Using H_k, Kalman filter gain is computed

$$K_k = P_k^- H_k^T (H_k P_k^- H_k^T + R_k)^{-1} \tag{2.28}$$

where P_k^- is the *a priori* time updated covariance of the state vector and R_k the measurement covariance matrix ($R_k = E[\nu\nu^T]$). Given the *a priori* state estimate $\hat{\mathbf{x}}_k^-$, actual measurements $\mathbf{z}_k$, the expected nonlinear measurements $\hat{\mathbf{z}}_k$ and the Kalman gain K_k the measurement update of the state can be completed

$$\hat{\mathbf{x}}_k = \hat{\mathbf{x}}_k^- + K_k(\mathbf{z}_k - \hat{\mathbf{z}}) \tag{2.29}$$

as well as the necessary state covariance updates from the current measurements

$$P_k = (I - K_k H_k) P_k^- \tag{2.30}$$

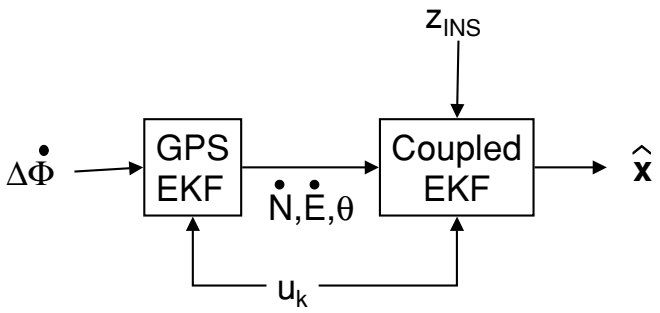

Figure 2-5: Cascaded filters indicated measurements and control inputs to each

The accuracy of the sensors as well as the measurement models effect the results of the extended Kalman Filter.

Note, to make the measurements of the velocity vector and heading from GPS available for comparison with the INS measurements, two filters were cascaded using synchronized measurements but the same time propagation equations. A schematic of the estimator design is shown in figure 2-5. The control inputs, u_k are supplied to the time propagator of each filter. The GPS EKF uses all of the available differential Doppler measurements, $\Delta\dot{\Phi}$, from the GPS receivers. The Coupled EKF uses INS measurements, z_{INS}, and GPS velocity results, $\dot{N}, \dot{E}, \theta$, to continuously compute a state estimate, $\hat{\mathbf{x}}$. Separate filters enabled a comparison of GPS methods alone, GPS methods with backup INS measurements and INS methods alone. The following sections identify the measurement models used for each filter.

GPS Measurement Model

Recall that for differential Doppler methods, the relative velocity between two users (j and b) is a measure of the projected velocity vector of each user onto their respective **los** vectors to the i^{th} common satellite

$$\Delta\dot{\phi}_j^i \;=\; \mathbf{los}_j^i \bullet \dot{\mathbf{x}}_{j,\text{GPS}} - \mathbf{los}_b^i \bullet \dot{\mathbf{x}}_{b,\text{GPS}} + \Delta\dot{\tau} + \dot{\nu}$$

If it is assumed that the satellites are far enough away and that the receivers are close enough together ($<$ 5km) that the **los** vectors are virtually parallel such that

equation 2.6 can be reduced to the form

$$\Delta\dot{\phi}_j^i \;=\; \mathbf{los}_b^i \bullet \Delta\dot{\mathbf{x}}_{j,\mathrm{GPS}} + \Delta\dot{\tau} + \dot{\nu} \tag{2.31}$$

The measurements are range rates in the relative reference frame. Typically, the base receiver is stationary to maintain a static reference for the Doppler measurement. Therefore, the relative measurement is a function of the actual precise velocity of the remote vehicle. Stacking N measurements together into a single vector $\mathbf{\Delta\dot{\Phi}}$, substituting the correct elements of the state vector and creating the corresponding geometry matrix G from the transposed **los** vectors forms the linear algebraic equation

$$\begin{aligned}\left[\mathbf{\Delta\dot{\Phi}}\right] &= \begin{bmatrix} \mathbf{los}^{1^T} & 1 \\ \mathbf{los}^{2^T} & 1 \\ \vdots & \\ \mathbf{los}^{N^T} & 1 \end{bmatrix} \begin{bmatrix} \dot{N} \\ \dot{E} \\ \dot{D} \\ \Delta\dot{\tau} \end{bmatrix} + \dot{\nu} \\ &\equiv \begin{bmatrix} G & \mathbf{1} \end{bmatrix} \begin{bmatrix} \dot{N} \\ \dot{E} \\ \dot{D} \\ \Delta\dot{\tau} \end{bmatrix} + \dot{\nu}\end{aligned} \tag{2.32}$$

where $\dot{D}$ is the relative vertical velocity of the ground vehicle and $\Delta\dot{\tau}$ is the relative clock drift rate. These two parameters are necessary to formulate the problem, but are of no interest to the current estimation result, therefore they are included as elements of the vector $\boldsymbol{\beta}$ in the state. In the second line of equation 2.33, the Nx3 matrix G is concatenated with the vector of ones on the right hand side creating the linear measurement matrix H_{GPS}. Typically 6–10 satellites are visible from surface of the earth, each providing range rate information in the direction of the line-of-sight.

After the estimate of the total velocity vector is updated, a GPS heading can be

formed by taking the four quadrant arctangent of the velocity components [7]

$$\theta_{GPS} = \arctan\left(\frac{\dot{E}}{\dot{N}}\right) \tag{2.33}$$

The value θ_{GPS} as solved from equation 2.33 follows the heading measurement convention of $(0, 2\pi)$ at north and increasing clockwise from above. However, the measurement is only useful when the vehicle is in motion.

Coupled Measurement Model

For the sensor bias estimation in the Coupled EKF, the precise North and East velocity results of the GPS estimation are supplied as measurements

$$z_{\dot{E},GPS} = \dot{E} + \nu_{\dot{E},GPS} \tag{2.34}$$

$$z_{\dot{N},GPS} = \dot{N} + \nu_{\dot{N},GPS} \tag{2.35}$$

The output of the GPS filter is an assumed unbiased velocity measurement in the N-E reference frame. Most linear factors that introduce errors are eliminated by using a single difference measurement.

The GPS heading measurement is supplied to the coupled filter assuming no contributing error sources besides white noise

$$z_{\theta,GPS} = \theta + \nu_{\theta,GPS} \tag{2.36}$$

Errors could be caused by side-slip of the ground vehicle. Research has shown that CDGPS methods with two antennas attached to a test vehicle can observe the difference between vehicle heading and velocity [42]. The constructed testbed showed no side-slip effects through any dynamic control therefore it was determined that the complexity of using more hardware and expanding the estimation would not be worth the benefit.

The previous measurements are taken only when the GPS receiver has constel-

lation visibility and able to track at least 4 signals. If GPS velocity and heading measurements are not supplied to the coupled filter, the vector of expected measurements $\hat{\mathbf{z}}_{\text{couple}}$ and the linearized matrix H_{couple} are reduced in size accordingly.

As mentioned in section 2.1.2, a compass measurement was used as the backup sensor when in a stationary position or during GPS signal occlusion. The measurement was assumed to include the actual value of the heading θ as well as a constant bias due to magnetic disturbances (i.e. the drive motor on the RC truck)

$$z_{\theta,INS} = \theta + \beta_\theta + \nu_{\theta,INS} \tag{2.37}$$

The β_θ term was added as another state vector element. During simultaneous measurements of GPS and the compass, the bias can be estimated and later used to correct the compass measurement at times when INS must operate alone.

To determine the path distance traveled during a time step, an encoder is attached to an axle of a rear wheel. The path divided by the wheel radius r generates a representation of the rotation of the wheel axle

$$z_{s,INS} = (\sqrt{(N_k - N_{k-1})^2 + (E_k - E_{k-1})^2} + \beta_s) r^{-1} + \nu_{s,INS} \tag{2.38}$$

Because of possible error in the radius measurement and/or because the actual path was laterally offset for the rigid body center of gravity, the bias term β_s was used to model the error of the encoder measurement. As with the compass, the bias term can be estimated during simultaneous GPS/INS measurements and can be used to correct the measurement while using INS alone. Equation 2.38 assumes a straight-line path connecting the previous position estimate, $k-1$, to the current value, k. A higher fidelity model could include a curvilinear path that uses change in heading as well as position. In the case of this research development, the measurement update periods are sufficiently short (nominally available at 5 Hz) such that the straight-line assumption appears to work well.

If the vehicle passes through the laser set-up described in section 2.1.3, a single position measurement can be input to the filter. All of the previous formulations exist

with the additional condition of the position measurement

$$z_N = N + \nu_{N,GPS} \tag{2.39}$$

$$z_E = E + \nu_{E,GPS} \tag{2.40}$$

It was assumed that no additional biases were observable in the position measurement and all measurement error (see table 2.1) was incorporated into the noise.

The parameters shown in the coupled measurement model equations not already present in the state vector $(N_{k-1}, E_{k-1}, \beta_\theta, \beta_s)$ were concatenated to become part of $\boldsymbol{\beta}$. Constants were assumed for all of the parameters therefore resulting in no changes due to dynamic propagation.

Note that the primary measurements observe the rate elements of the state vector. The measurement limitation causes the position covariance to drift to larger values as the filter progresses forward in time. When using CDGPS, the position covariance quickly converges to provide precise state estimation regardless of elapsed filter time. In the case when GPS Doppler is used, the position covariance grows very slowly. For the short term applications used in this research, the drift rates are small enough to achieve good position accuracy but any situation requiring long estimation time will have much better position error results with CDGPS.

Due to larger expected noise values of the inertial sensors, the covariance drifts much faster when only INS is available. The only improvement of position covariance is through the laser beam position update where the measurement model quickly reduces the position covariance over one step providing some increased confidence in the position state estimate. Essentially, all of the previous position state information is eliminated and the measurement update causes a noticeable jump in the estimated path (see results in Chapter 4).

2.3 Estimation Conclusions

By included estimated sensor errors in the measurement model, the integrity of the total GPS/INS sensor system could be improved when GPS signals are unavailable or if blocked. If greater bandwidth is desired for dynamic observability of the overall filter, the frequency of the INS could be significantly faster than that of GPS. Updates on the bias estimation would then be limited to only those times when both measurement capabilities were available. For the current application, the INS measurement system was to be used to augment the robustness of the GPS velocity estimation algorithm. Results of the designed filter are presented in chapter 4.

Chapter 3

Vehicle Control

While the estimation methods are important for state determination, the overall objective of creating an autonomous fleet of roving vehicles requires development of algorithms to perform two-dimensional vehicle control. It is assumed that a set of path waypoints is supplied to each vehicle in the testbed requesting specific maneuvers. The formulation of the path is beyond the scope of this thesis and can be found in Ref. [45]. The motivation for vehicle control is to validate hardware-in-the-loop experiments of real-time path planning. A nested-loop control architecture is designed. This chapter discusses the low-level control of speed and heading for the ground vehicle. It concludes with algorithms to create reference inputs of heading and speed to complete closed-loop path-following control.

3.1 Speed Control

The forward motion of the test vehicle hardware is driven by a digital input. This value is passed to a micro-controller which converts to a pulse width modulated (PWM) signal that drives a servo. This then turns a potentiometer arm which drives the DC motor voltage. (Actual components and manufacturers are identified in Appendix A).

The closed-loop control system block diagram is shown in figure 3-1. The plant was modeled as a first-order lag with 1–2 second time constant. A lead-lag compensator

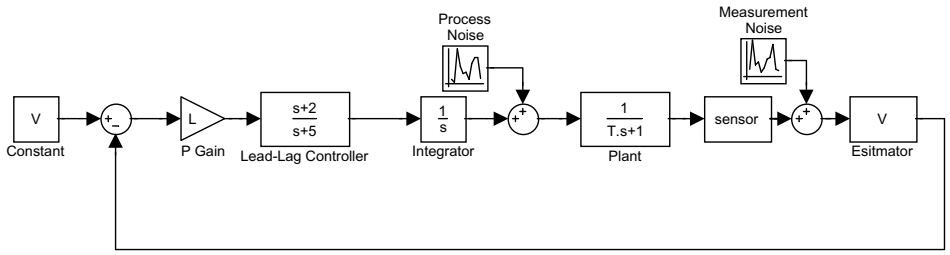

Figure 3-1: Speed closed-loop control block diagram

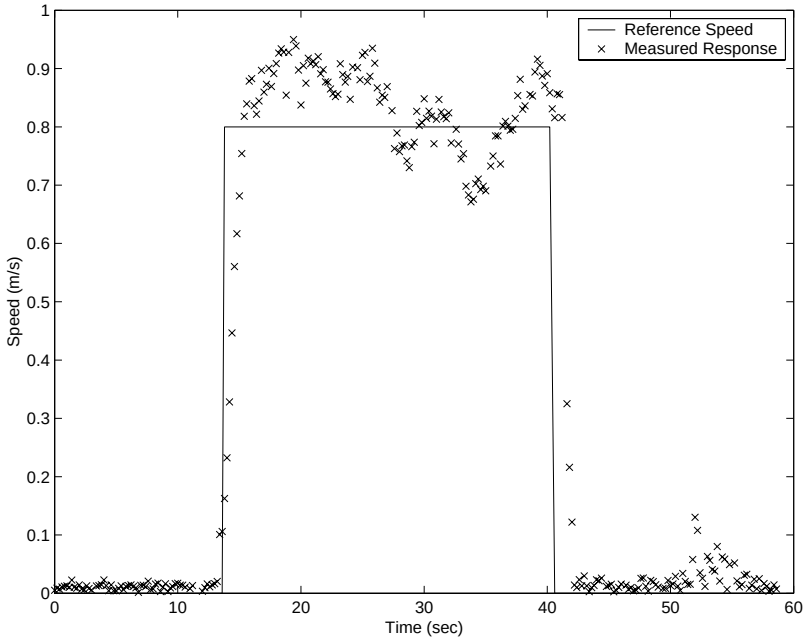

Figure 3-2: Speed closed-loop control response

with integral action is employed. The final compensator design is a pole at -5 and a zero at -2. The overall proportional gain of the controller L was tuned high enough to produce fast response of the system. However, consideration was taken to be sure the value was low enough that control would not request input saturation even at maximum closed-loop error.

Because the measurements are made at discrete times, the actual algorithm is programmed using digital control techniques, with a zero-order hold on a 5 Hz sampling rate [38]. Figure 3-2 indicates the controller performance, $\times$, for a constant input reference speed (solid line). Fast response to the step input is observed with an overshoot of speed. Some oscillation in the response is expected since the compensator design produced closed-loop poles off of the negative real axis. Longitudinal speed

disturbances are caused by side-slip of the front steering wheels and undulations in the surface. The results in figure 3-2 indicate the mean error is only 0.036m/s with a standard deviation of 0.069m/s. These results are satisfactory for closed-loop control of longitudinal speed for the ground vehicle testbed.

3.2 Heading Control

The rigid body heading is controlled by steering the front wheels with servos, per the Ellis bicycle model [40]. The heading rate equation 2.21 from the dynamics model in section 2.2.1 indicates the plant for heading control is nonlinear

$$\dot{\theta}_k \quad = \quad \frac{\| \mathbf{V}_k \|}{L} \tan \delta$$

Another contributing factor not included in equation 3.1 is an actuation saturation limiting of δ to $\approx \pm 20^\circ$. When operating around the linearized region, the plant can be modeled as a first-order lag. This can be stabilized by a proportional controller.

Separate control gains, K_r and K_l, were defined for positive and negative error to compensate for the non-uniform response of the left/right turning mechanism. Similar to the speed control gain, the value was set high enough that the response time would be 1–2 seconds given a step input ($\Delta\theta > 25^\circ$). An upper limit on the gain was determined in order not to force the controller to immediately approach the mechanical saturation limits. All of the nonlinear factors contributed to a minimum turn radius of $\approx$ 2m (maximum $\dot{\theta} \approx 75 - 85^\circ$/s) for the ground vehicle.

Further consideration was also made for the phase-wrap of the heading that occurs at 0 and 2π. It was assumed that the minimum and maximum bound of the heading error could be $\pm\pi$, respectively. By forcing the error bounds, differences around the nonlinear wrap point would not result in vehicle control commanding an entire circle to be traversed.

Figure 3-3 shows the performance of the closed-loop controller with large step changes of the reference heading. The response and settling time met the control

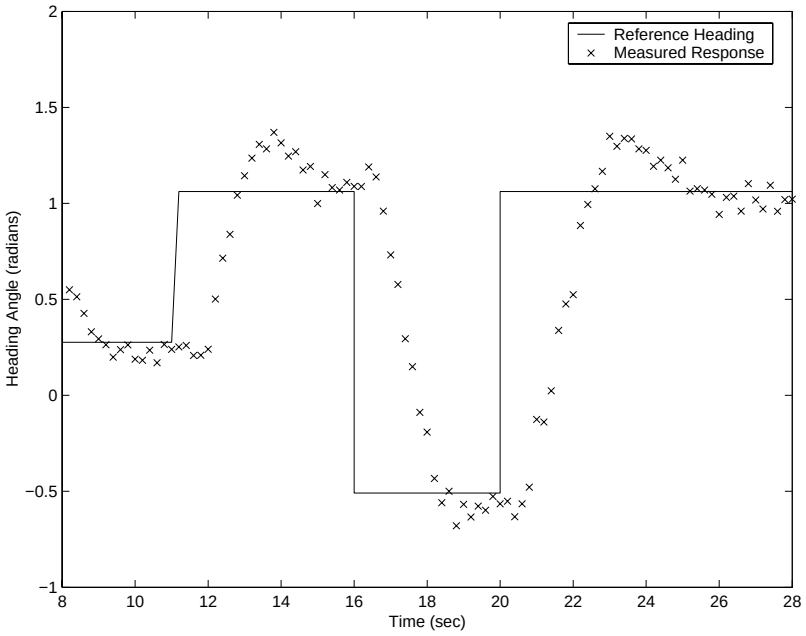

Figure 3-3: Heading closed-loop control response

requirements ($\Delta\theta_{ref} = 45°$ at 11 s; $-90°$ at 16 s; and $90°$ at 20 s). Under typical operation, the reference heading has a more continuous change ($\dot{\theta} < 20°/\text{sec}$), resulting in better tracking of the closed-loop heading control.

3.3 Position Control

With the low-level controllers designed, an outer control loop was developed to use the two desired inputs ($\|\mathbf{V}\|_d, \theta_d$) to create a nested-loop feedback control system, shown in figure 3-4. The outer-loop performance hinges on the satisfactory control of the speed and heading states by the low-level feedback loop. This section presents outer-loop control designs used to complete the position control requirement.

It is assumed that all planned paths supplied to the testbed provide waypoint locations, as well as all components of the state vector. The desire is not only to reach a particular location, but to reach the location with a desired heading such that a continuous smooth path may be traveled. The actual path trajectories were designed using receding horizon control with mixed-integer linear programming [45]. The path planning method is able to consider dynamic constraints such as a nominal

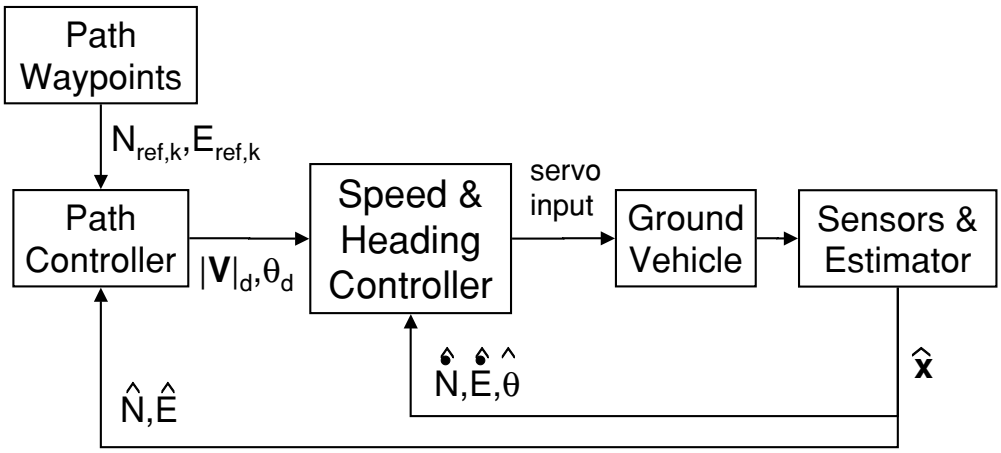

Figure 3-4: Ground vehicle closed-loop position control

constant speed and minimum turn radius such that the formulated paths are within the vehicle dynamic capability. Feedback of the completed path can also be provided to the path generation algorithm to determine if a new plan must be designed and executed to meet the overall objectives.

3.3.1 Heading provided by plan

In this control scheme, the speed and heading references are taken directly from the plan synchronized to GPS time. Assuming that the low-level controllers were able to create dynamic performance equal to the model used for planning, the resulting motion would naturally generate the requested path. To maintain a smooth change in heading between waypoints, the control computer used a linear interpolation between the current heading direction and the desired future heading

$$\theta_d = \theta_{k-1} + (\theta_k - \theta_{k-1})\frac{\hat{t} - t_{k-1}}{t_k - t_{k-1}} \tag{3.1}$$

where θ_{k-1} is the heading at the previous achieved waypoint; θ_k is the desired heading at the next target location; $\hat{t}$ is the current estimate of GPS time; t_{k-1} and t_k are the planned times when the vehicle should be at the previous and future waypoints, respectively. Once again, care must be taken when desired headings from the plan cross the phase wrap of the vehicle heading. Nominally, the absolute differences in

heading should be less than π, therefore the headings supplied by the plan would sometimes be unwrapped for calculating the interpolated heading.

Communication was set up to report the position estimate to the planning computer. If the vehicle trajectory deviated too far from the planned path according to the timing synchronization, a new plan would be generated given the current state conditions and desired goal point. The implementation of this algorithm allowed the planning computer to close the outer-loop on position control. From the ground vehicle perspective, supplied reference heading was simple open-loop control.

Due to model mismatch, actual vehicle paths did not follow the requested plans requiring new plans to be created. Delays in path re-generation led to poor ability to correct deviations from the nominal path. It was determined that the outer position loop must be closed at a much faster rate in order to achieve adequate results for accurate path following maneuvers.

3.3.2 Proportional position control

The first attempt at autonomous testbed closed-loop position control was to use proportional position control to point the vehicle to the next waypoint. The desired heading was calculated from the current position estimate to the next position in the plan

$$\theta_d = \arctan\left(\frac{E_k - \hat{E}}{N_k - \hat{N}}\right) \tag{3.2}$$

where (E_k, N_k) is the coordinate of the desired waypoint and $(\hat{E}, \hat{N})$ is the current estimate of vehicle position. Figure 3-5 shows these vectors in the reference frame with previous and future waypoint locations indicated. The calculation of equation 3.2 was computed at the nominal measurement period of the real-time filter, meaning that both the inner low-level loops and the outer position loop were being closed at the same rate. When the position comes within a decision range around the plan step, indicated by the dashed circles, the plan step was incremented to begin maneuvering

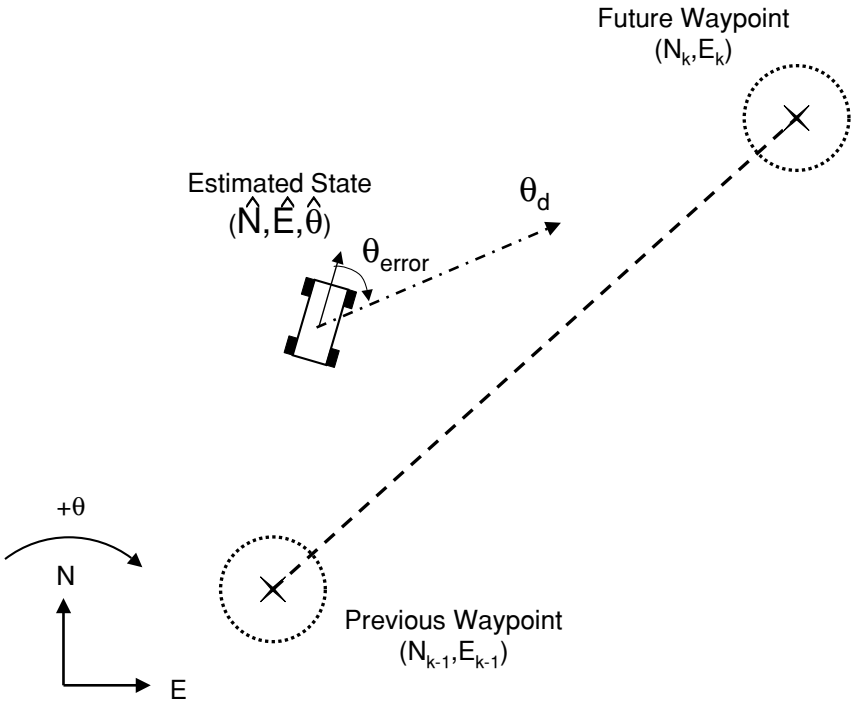

Figure 3-5: Proportional control model; Reference heading determined by vector from current position to desired position

to the next waypoint. Note the benefit of using a proportional position control scheme is that most of the control effort is used at the beginning of the maneuver to change the heading toward the desired waypoint. Once on the straight line path between current position and the target, the effort in maintaining the heading is minimal. However, this method only works well only when the deviation from the path is relatively small.

Because the limited turning radius, the ability to adjust laterally along the path degrades rapidly as the vehicles gets closer to the waypoint objective. When adequate path length is not available to correct the lateral error, the generated reference heading acts aggressively to adjust the vehicle orientation. Often, the desired heading differs substantially from the nominal path trajectory resulting in very sharp turns. In some cases, the reference heading was greater than 90° causing steering command saturation resulting in the vehicle circling around the waypoint objective. If the minimum turn radius is larger than the decision range, proportional position control will forever drive circles until commanded otherwise. When a waypoint *is* reached, the vehicle state may not match the original plan therefore making it more difficult

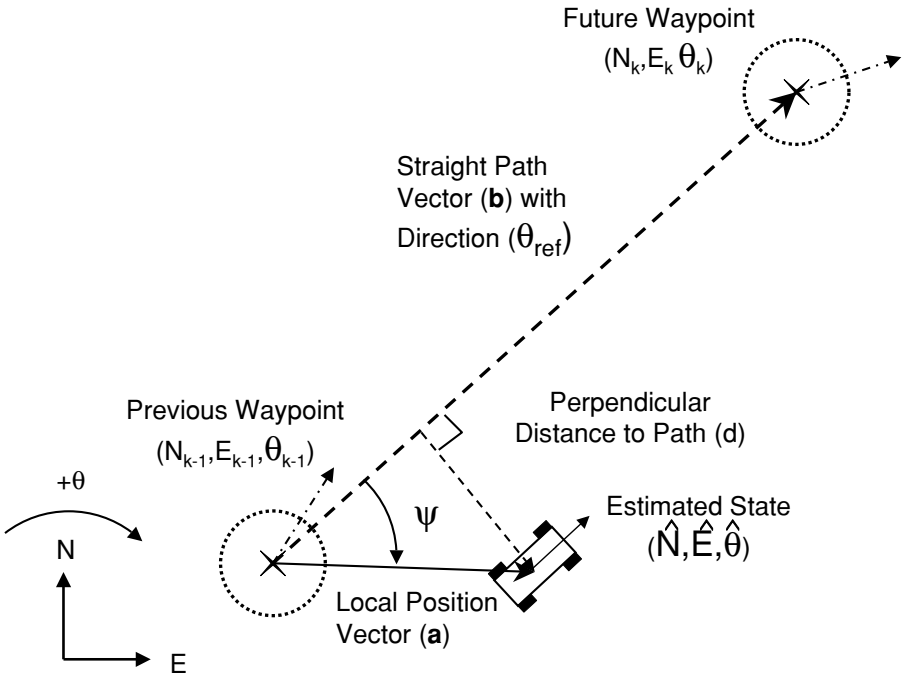

Figure 3-6: Autopilot ground track control model; Minimize lateral path error

to reach the next desired waypoint.

It was determined that the proportional control algorithm works very well for waypoints with significant separation distances (> 3 meters) or when the vehicle can move at a slow speed (allowing enough path time to adjust laterally). Since supplied paths use small step-sizes, < 1 meter, the proportional position control algorithm does not provide satisfactory closed-loop position control results.

3.3.3 Heading Autopilot with ground track control

For effective path following, the heading of the vehicle should nominally match the requested heading from the plan at each waypoint. To better achieve this objective, the ground track position control algorithm attempts to match a reference heading while minimizing the lateral distance to the path connecting previous and future waypoints [51].

The perpendicular distance of the estimate from the straight-line planned path, shown as d in figure 3-6, is measurable from the known parameters of the plan and current position estimate. First, vectors from the previous planned point to the current

position estimate and future desired position, **a** and **b** respectively, are determined.

$$\mathbf{a} = \begin{bmatrix} \hat{N} \\ \hat{E} \end{bmatrix} - \begin{bmatrix} N_{k-1} \\ E_{k-1} \end{bmatrix} \tag{3.3}$$

$$\mathbf{b} = \begin{bmatrix} N_k \\ E_k \end{bmatrix} - \begin{bmatrix} N_{k-1} \\ E_{k-1} \end{bmatrix} \tag{3.4}$$

The angle, ψ, between vectors **a** and **b** is measured from the straight-line path to the localized position estimate with the sign being solved from the normalized determinant of the two vectors

$$\psi = \frac{\det[\mathbf{a}, \mathbf{b}]}{\| \det[\mathbf{a}, \mathbf{b}] \|} \arccos\left(\frac{\mathbf{a} \bullet \mathbf{b}}{\| \mathbf{a} \| \| \mathbf{b} \|} \right) \tag{3.5}$$

The value of d is the component of the vector **a** perpendicular to the path vector **b** and computed as

$$d = \| \mathbf{a} \| \sin(\psi) \tag{3.6}$$

The sign of d when the vehicle is on the left side of the path is negative and positive for path following errors on the right side. The rate which d changes is a function of the vehicle speed and the difference between actual heading, θ, and the direction of vector **b**, θ_{ref}

$$\dot{d} = \| \mathbf{v}_{ref} \| \sin(\theta - \theta_{ref}) \tag{3.7}$$

When θ is greater than θ_{ref}, the sign of $\dot{d}$ is positive making the vehicle move to the right with respect to the desired path. When the opposite is true, the vehicle position tends to drift to the left of the planned straight-line trajectory. If the actual heading and reference heading were to always match, d would never change and perfect path following would occur. By incorporating the relationship between reference heading and rate of return to path, a balance can be created between the two requirements

to produce a desired heading, θ_d.

Assuming the difference between the reference and desired orientation is small, the sine function in equation 3.7 can be approximated by the linear relationship

$$\sin(\theta_d - \theta_{ref}) \approx (\theta_d - \theta_{ref}) \tag{3.8}$$

which can be substituted into equation 3.7. Because d is a simple integrator, a lag compensator with a time constant $\tau\|\mathbf{v}\|_d$ is used to calculate the desired heading necessary to adequately control the lateral path distance

$$\theta_d = \theta_{ref} + \frac{d}{\tau \parallel \mathbf{v}_{ref} \parallel} \tag{3.9}$$

The result of equation 3.6 can be substituted into equation 3.9 to form the new desired heading to be used in order for the vehicle to follow the planned path

$$\theta_d = \theta_{ref} + \frac{\parallel \mathbf{a} \parallel \sin(\psi)}{\tau \parallel \mathbf{v}_{ref} \parallel} \tag{3.10}$$

The ground track algorithm computations were calculated at the same frequency as the low-level controllers (5 Hz). Early experiments indicated that values of τ less than 1 second made the proportional gain too sensitive to the lateral path error inducing oscillation across the path. Values of τ were selected ($\approx 1.1 - 2.0$ seconds) to give the vehicle approximately half of the time between waypoints to return to the path. Due to the included decision range around each waypoint, overshoot of the path during plan increment steps was minimal.

To add robustness to the control scheme, the along path distance was used to determine when a waypoint is passed by the test vehicle. The value can be calculated from the projection of vector **a** onto **b**. When the vehicle does not pass within the decision circle of the desired waypoint, but the along track distance is longer than the straight-line path

$$\frac{\mathbf{a} \bullet \mathbf{b}}{\|\mathbf{b}\|} > \|\mathbf{b}\| \tag{3.11}$$

the waypoints are incremented to the next step in the plan. This robust addition for stepping ahead in the plan eliminates the waypoint circling present in proportional position control.

The ground track algorithm provides desired commands to the low-level controller thereby creating a path that includes consideration of all of the desired elements of the state vector – position, speed and heading. The performance is a significant enhancement over proportional position control, which operated solely on the vehicle position without regard to the rest of the state. Thus, the autopilot design was the algorithm implemented in the testbed for the path following results presented in Chapter 4.

3.4 Control Conclusions

To create complete controllability of the autonomous testbed, a nested-loop control method was required. Feedback control was designed for fast response of speed and heading of the test vehicle. Using the reference inputs to the low-level controllers, the outer-loop for position control could be closed. The designed algorithm for feedback control of path following must take into account the nonlinear effects of position modeling. Achieving position objectives is the primary focus, yet other parameters of the vehicle state must be considered for a smooth path following. For the current application, it was found that the autopilot ground track algorithm provided the best results for autonomous closed-loop position control for path following.

Chapter 4

Experimental Results

This chapter presents results of the estimation and control algorithms outlined in the previous chapters. Performance metrics are compared for both the estimation results and the control of the test vehicle. Also, hardware selection and construction is addressed for the multi-vehicle testbed.

4.1 Hardware

4.1.1 GPS Receivers

The GPS hardware selected for this experiment was the Canadian Marconi Company Superstar^{TM} receiver. The twelve channel receiver provides both raw Code phase and carrier phase measurements for all tracked satellites. This particular model was selected due to the previous success using the Zarlink (previously Mitel/Plessey) GPS chip-set. However, unlike previous designs, we did not have access to the receiver source code, thereby eliminating any possibility of modifying the tracking loop or specific receiver abilities. With 12 available channels to track GPS signals, any satellites in the NAVSTAR constellation above the horizon can be observed.

The raw carrier measurements were available at frequencies of 1, 2, 5, and 10 Hz. Other receiver parameters such as channel assignment, pseudorange solution, and satellite ephemeris are only provided once a second since they are not necessary for

a rapid solution. All decoding of the serial communication was specified in the GPS users manual [32]. In order to simulate the Doppler, which is sometimes provided as part of the communication message from a receiver, the carrier phase measurements were differentiated by the estimation computer and assumed to be constant over the measurement time interval. (Had access been granted to the onboard receiver source code, the Doppler value of the tracking filter would have been included in the communication messages). While the 10 Hz update rate would be beneficial for greatest bandwidth, the receiver was not able to provide reliable communication of the raw phase data at this rate. Experiments showed that one out of every ten measurements would be lost, even at the maximum baud rate of 19.2 Kb/sec. Each loss resulted in a backup of data on the serial communication thereby increasing the measurement delay during the experiment. Eventually when the first-in first-out (FIFO) buffer become full on the serial port, significant portions of raw phase message were lost making the measurement invalid. The error was due to the other messages taking the required communications bandwidth. In order not to lose transmitted data or over-fill the communication buffers, the measurement rate was reduced to 5 Hz.

Other equipment necessary to work with the receiver was a powered GPS antenna from Maxcom that gave a 26 dB gain of the GPS signal. Also an interface board was produced to include a power converter, reset button and an integrated circuit to change the communication levels from TTL (to/from the receiver) to the RS-232 levels necessary for communication with a computer serial port.

4.1.2 Base Station Computing

A laptop with a 700MHz Celeron processor was selected to compute the estimation and control algorithms developed in previous chapters. Rather than attempt to distribute the individual vehicle computation, it was decided to have a single-point interface between the user and the entire fleet. This eliminated additional payload hardware required for onboard computing and offered full visibility to the fleet estimation and control. Operation usually centered around the base-station GPS receiver location in order to eliminate the need for remote communication to/from the device.

An MS-DOS executable was created to conduct all of the communication via serial and parallel ports as well as compute the estimation and control results. USB to serial port adapters from Belkin with MS-DOS support were used to quickly expand the number of available ports to conduct communication. Each remote device (i.e. base station receiver or ground vehicle) was able to have a dedicated port for sending commands and receiving data. Estimation methods were common between all fleet vehicles, but individual state vectors were created for each. Similarly, control of individual vehicles could be calculated and sent without disrupting the other members of the fleet.

4.1.3 Transportation Equipment

Research testbeds were constructed previously to carry very similar GPS equipment payloads [44]. The Tamiya Mammoth Dump truck, shown in figure 4-1, was selected as the transport vehicle for the new multi-vehicle testbed due to its low cost, high gear ratio for slower maximum speed (compared to racing RC vehicles), and specified payload capability of 4 kilograms. The gear ratio (91:1) indicated that significant torque could be supplied to the drive axles for better controllability at all speeds. Furthermore, the included dump bed was a useful device for holding the necessary experimentation equipment. The strong aluminum frame and dual coil-and-leaf spring suspension provided a sturdy platform to carry the experimental hardware. The full weight of all hardware components was well within the limits of the payload capacity such that future experiments could expand the payload capability (i.e. onboard computing, pseudolites). Additional hardware required were two servos necessary for turning the potentiometer for the motor input and turning the front wheels for steering. The servos and magnetic motor were able to run from the single 8V Ni-Cd battery carried in the vehicle chassis.

Figure 4-1: Tamiya Mammoth Dump Truck with electronics payload

4.1.4 Micro-Controller

Controlling the rotation of the servos required changing a 50 Hz Pulse Width Modulated (PWM) signal. Since the ultimate design for the testbed was to have autonomously controlled vehicles, individual micro-controllers capable of generating the PWM were included in the truck payload. The Motorola HC11 micro-controller has a single serial port and 5 additional input/output ports for both reading and producing digital signals. The serial port allowed RS-232 communication with the base station computer. A simple interface was desired between the base station estimation/control computer and actual adjustment of speed and steering of the vehicle. Once the computer produced a desired percentage of servo turn, a data message was created and transmitted to the micro-controller. A program was developed for the micro-controller to receive the commands in the message and translate them into output PWM signals.

Using the additional I/O ports, the micro-controller was also able to double its capability as a data acquisition device for the inertial measurement sensors. Sending

clock signals and reading the output pins of a Vector 2X compass enabled the HC11 to have an analog measurement of the magnetic heading of the vehicle. The value could then be converted to a digital measurement and reported to the base station. Measurement noise from the compass was $\approx 2^{\circ}$. To measure longitudinal displacement, a 50 pulse per revolution optical encoder was attached to the rear axle of the vehicle. Two square wave signals were then observed by the HC11 to count rotations. The two were out of phase by 90° such that one would lead in clockwise rotation but follow when rotating in reverse. The A/D sampling was fast enough that only single pulses were ever missed resulting in a longitudinal displacement measurement noise of 0.009 m. Each of these devices are capable of sensing individual components of the state of the vehicle, however as discussed in Chapter 2 each can have biased errors that are not related to the measurement noise value.

4.1.5 Communication

In order to allow the vehicle full mobility away from the base station computer, remote communication devices were necessary to transmit and receive the RS-232 data signals. High integrity radio modems were purchased to replicate the null-modem cable connection required for communication of two computers on a serial port. The Data-Linc group SRM6000, 900MHz frequency hopping radio modems were selected due to the excellent performance previously demonstrated during highly dynamic and heavy occlusion environments [42]. Since only the single communication link was available between the base station and a remote vehicle, the messages from the remote GPS receiver and HC11 were required to be transmitted on the same signal line. The maximum baud rate of the HC11 micro-controller was found to be 9.6 Kb/sec, thereby eliminating the possibility for both devices to transmit at 19.2 Kb/sec on a simple switching timer. The B&B Electronics Buffered Smart Switch device was used to combine RS-232 communication from the two separate devices and transmit on a single port [57]. The Smart Switch buffered data from a device until the communication link to the base station was available and then transmitted until the buffer was emptied. By adding a header to data coming from

each of the remote devices, message components received at the base station could be sorted between those coming from the GPS receiver and those from the HC11 micro-controller. Since the new header and micro-controller information was being added to the communication message, the baud rate between the truck and the base station was increased to 38.4 Kb/sec. Messages from the base station were preceded by a header indicating the desired destination device for communication and broadcast to all connected ports.

4.1.6 Power

All electrical components in this section were powered by 8V Ni-Cd batteries with 2000 to 3000 mA-Hrs per full charge. A single battery was required for both the receiver and truck motor, and a two battery set in series for the micro-controller and communication boxes. Typical operation of a fully powered vehicle was 20-30 minutes depending on the length of driving experiments were conducted and duration of high bandwidth communication between the vehicle and the base station. Each battery also added significant weight to the total payload and was considered in vehicle selection.

4.1.7 Hardware connections

A schematic showing all of the connections between the separate hardware components is given in figure 4-2. The HC11 box not only contains the micro-controller but the 12V power regulator as well. Power is supplied from two 8V batteries connected in series. The dash dot lines indicate co-axial power cables with BNC and appropriate DC jacks on the opposite end. When the box is turned to the "on" position, all of the components become active, as indicated by the power LED's on the radio modem and the Smart Switch.

Any continuous lines are straight ribbon cables between the "D" connectors and other sockets. A fifteen pin connector is used between the compass device and the HC11. A 9 pin connection between the truck and HC11 receives signals from the axle

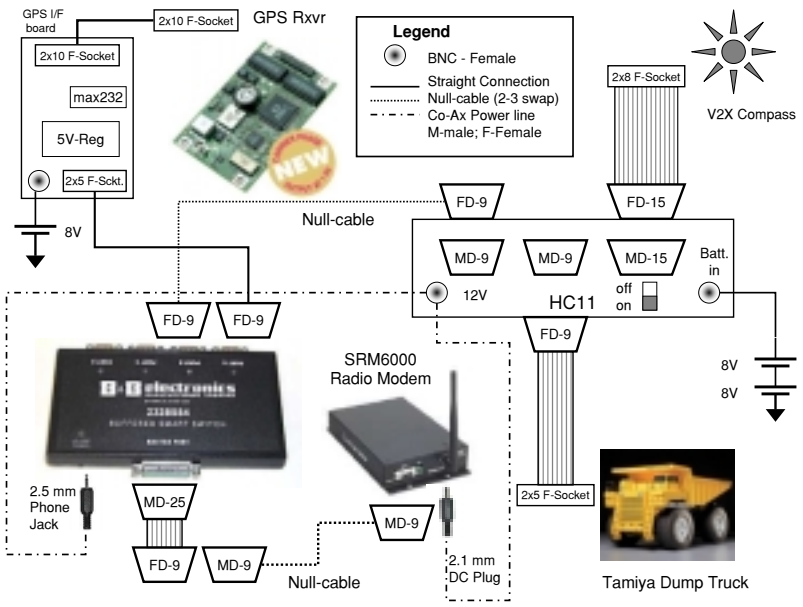

Figure 4-2: Hardware connections for individual truck components

encoder and transmits the PWM for the servo control. The other dashed lines between female D-9 connectors are null-modem lines where pins 2-3 are swapped to allow communication computers to both transmit and receive messages simultaneously. The GPS interface board contains some circuitry to allow a separate power supply that will not cycle when the HC11 needs to be reset as well as a max232 chip to change communication levels between RS-232 and TTL. All hardware part numbers, manufacturers and costs are given in Appendix A.

4.2 Receiver Measurement Tests

Initial experimentation was conducted to measure the latency of the GPS measurements as well as the accuracy of the estimation velocity. The base station computer clock was synchronized to Universal Time Command (UTC) available from NIST (National Institute of Standards and Technology). It was found that the delay between reported time on the raw GPS data had a maximum latency of 60 msec with respect to this well-synchronized computer clock. The measurement latency is negligible and measurements were assumed instantaneous to the GPS time.

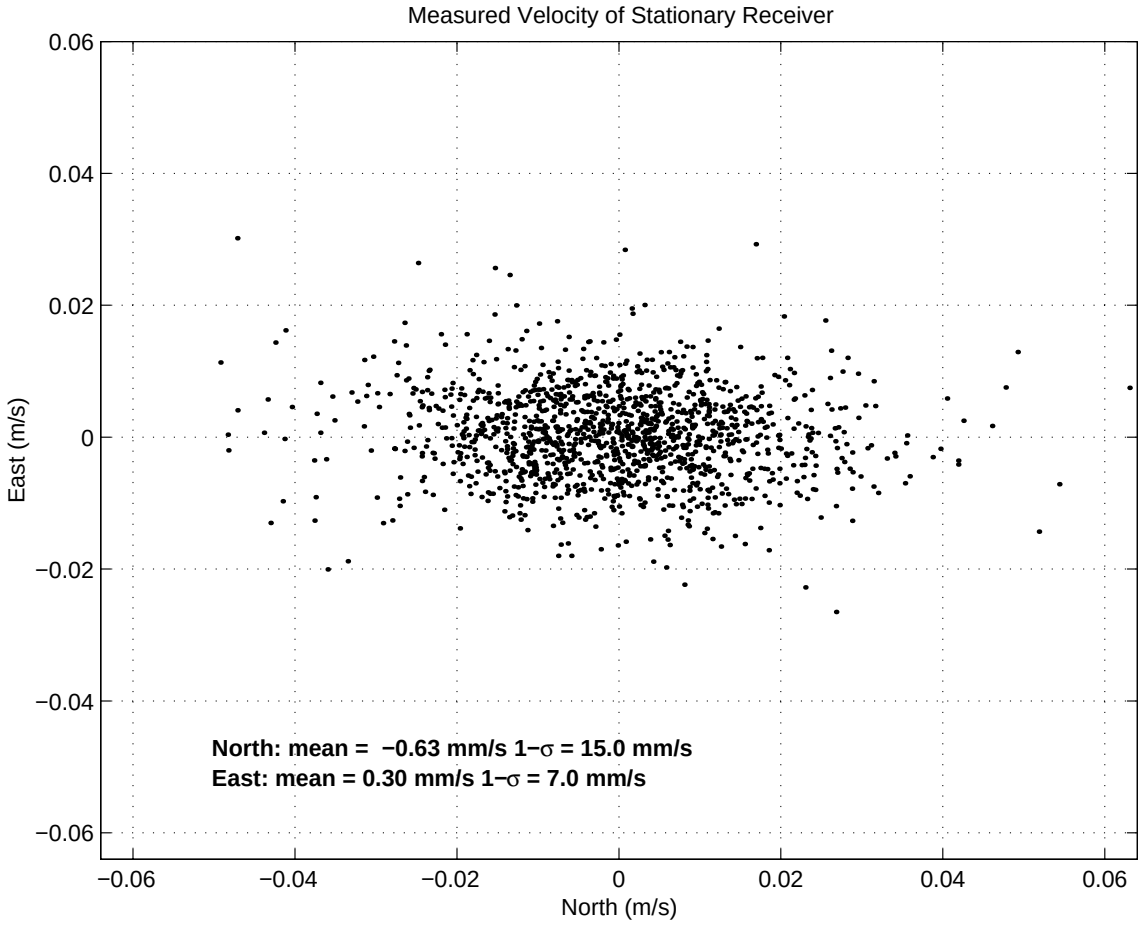

Figure 4-3: DGPS Velocity Measurements of a Stationary Antenna

To determine the potential solution noise, two receivers computing differential Doppler measurements were tested with stationary antennas. The WLS solution was calculated for each time step of the experiment

$$\begin{bmatrix} \dot{\mathbf{x}}_{GPS} \\ \dot{\tau} \end{bmatrix} = (H^T R^{-1} H)^{-1} H^T R^{-1} \begin{bmatrix} \Delta\dot{\Phi} \end{bmatrix} \tag{4.1}$$

A scatter plot of estimated velocity in reference frame coordinates is shown in figure 4-3 with the mean and standard deviation shown. The results indicate that the estimate has a very small bias which means the position error will not grow very rapidly when integrating the velocity. Also, the standard deviation shows an improvement over velocity estimation methods that use differentiated CDGPS position solutions [23].

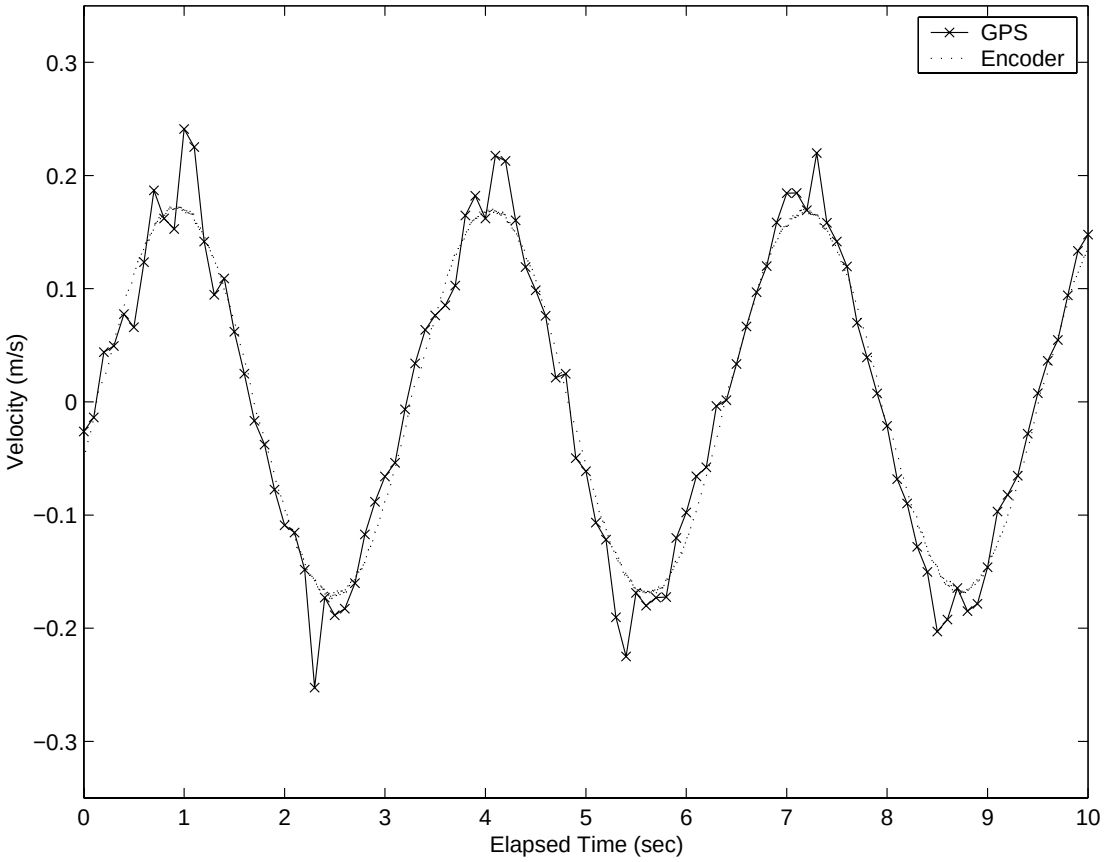

Figure 4-4: Velocity comparison of GPS WLS Doppler solution versus Pendulum speed

A final comparison test was conducted to verify dynamic velocity estimation prior to including the SuperStar^{TM} receiver in the vehicle testbed. One of the antennas was placed on the top of a pendulum with a period of approximately 3 seconds. The mounting point was 0.62 m above the pivot and would induce repeatable velocity values. A high fidelity 2000 pulse per revolution encoder was used to measure the rotation rate of the pendulum with a 100 KHz sample rate DAQ card. A comparison of the two velocity measurements is shown in figure 4-4. (Synchronization between the high bandwidth encoder and the GPS receiver proved too difficult for individual point comparison.) The two velocities are almost identical except at the peaks of the sinusoid. This error was a result of the WLS nature of the solution, since there was no smoothing or filtering of the data. If a dynamic model had been included to

form recursive Kalman filter estimation, such peaks in the measurement noise could be reduced. Given the good results of both the stationary and pendulum tests, the receiver was believed to have the integrity for use in dynamic vehicle testing as well as provide a baseline for future estimation comparison.

4.3 Dynamic Testing of Velocity Integration

In order to compare integrated velocity estimation to CDGPS results, testing was conducted on a parking garage rooftop using differential Doppler GPS. The primary focus was to determine whether the GPS velocity vector could be integrated over large distances and different dynamic conditions, yet still provide precise position information. Similar to the first CDGPS experiments discussed in Ref. [42], a car was mounted with a GPS antenna and receiver. The vehicle started at rest in a marked location where the measurements were recorded and the real-time WLS solution was calculated. Following the maneuver, the car returned to the starting location so that initial and final position values could be compared.

The run presented in Figure 4-5 indicates an X at the starting location and the O shows the final position. Three laps were completed at approximately 15-20 mph while attempting to follow the same nominal path around the test area. The actual forward position of the car was always returned to the same location by having a laser point to a specific location on the vehicle both at the start and end of the maneuver. The lateral position and heading errors were measured and recorded so that they could be compared with the estimated values. The total time for the three laps was 142 seconds with the final position estimation accuracy of 4.3 cm east and 28 cm south indicating a position error drift rate of 2 mm/s. A close-up of the estimation start and finish is shown in Figure 4-6. The three paths appear to travel through the origin with the final position drifting significantly south. Control error to the north cancels the position error drift to the south making all tracks appear co-linear until the final position is reached. The GPS Error in Figure 4-5 is the difference between the final position estimate and the actual antenna displacement measured

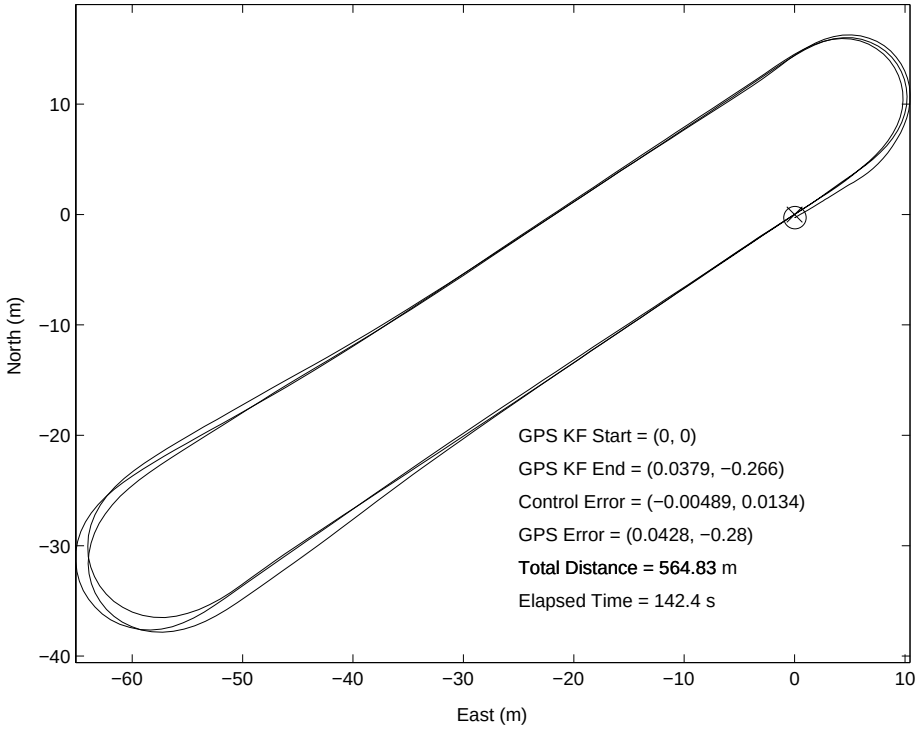

Figure 4-5: Integrated GPS velocity from differential Doppler measurements

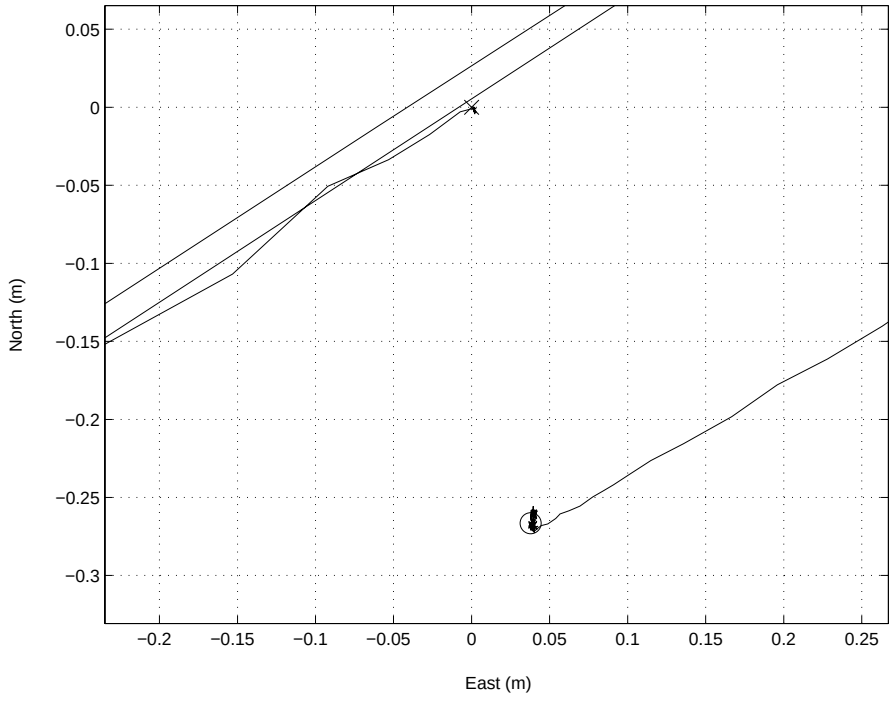

Figure 4-6: Close-up of start/end of figure 4-5

after the maneuver. While not as precise as the CDGPS approach, this demonstrates that integrating the accurate velocity data can be used to obtain very good position estimates at least over a short time periods.

4.4 Bias Estimation Results

The results of the bias estimation method using the complete set of hardware (truck, GPS receiver, HC11, communication system) are presented here. The objective was to drive a near oval path while passing under a metallic bridge and through the laser beam set-up described in section 2.1.3 and then return the vehicle to the original position. Control for the tested maneuvers was operated by manual input from the base station computer. By driving under the bridge, GPS signals were occluded for 2–10 seconds during which time the estimator only recorded information from the INS sensors. The laser positioning device was constructed with tripods holding the laser pen transmitters and solar cell receivers. The status of the laser devices was read by the controlling computer parallel port. Measurements from all of the devices were tagged with timing information and recorded. During post-processing, separate filters were run on the measurement data sets to compare robustness and accuracy of the following: GPS stand-alone estimation; INS stand-alone estimation; Coupled GPS/INS with bias errors included in INS sensor models; Coupled GPS/INS without sensor errors modeled.

Figure 4-7 shows a complete maneuver of the vehicle through the experimental section. The solid line with dots indicates the position solutions of the GPS only system as the maneuver was traversed. The rectangle near (2,6) indicates where a metal bridge was constructed to occlude the GPS signals to the receiver. Note that the GPS position solution is absent in this area. The dash-dot line shows how an INS only system estimates position after passing under the bridge. When the INS stand-alone estimator is started from the origin, the drift is so large that direct comparison is nearly impossible. The solid line represents a coupled estimator that does not include sensor biases in the measurement model. Simultaneous measurements for this filter

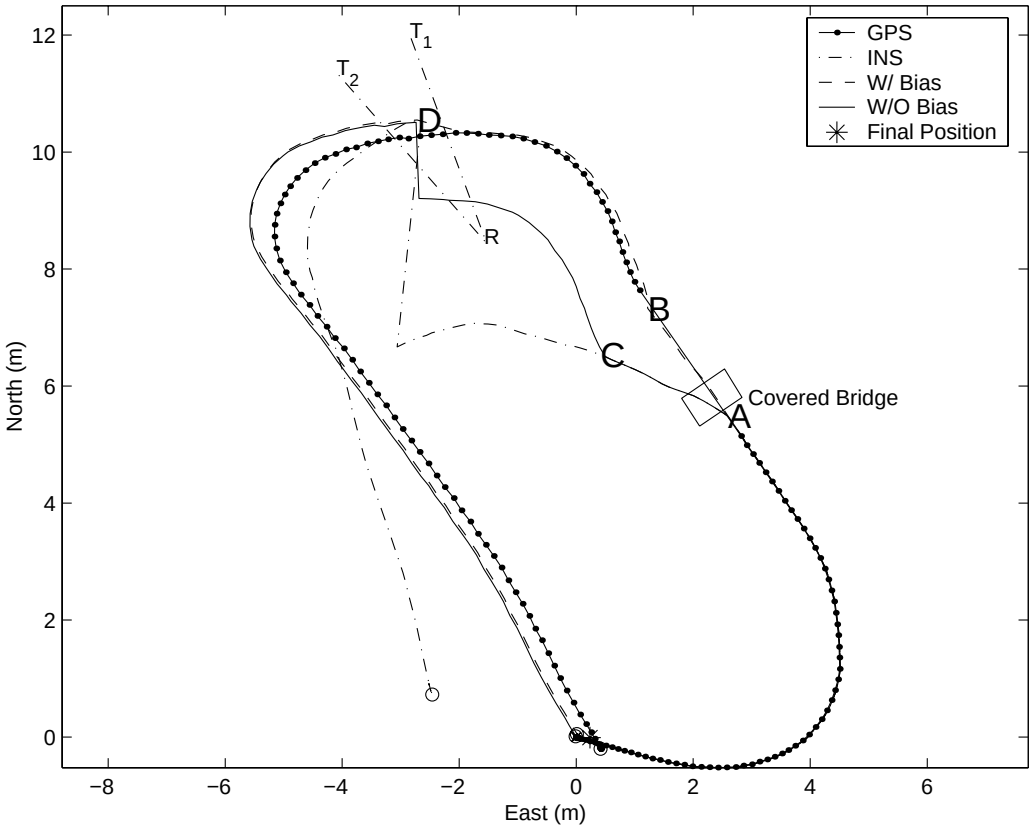

Figure 4-7: Position results of GPS and Coupled EKF - Run 33

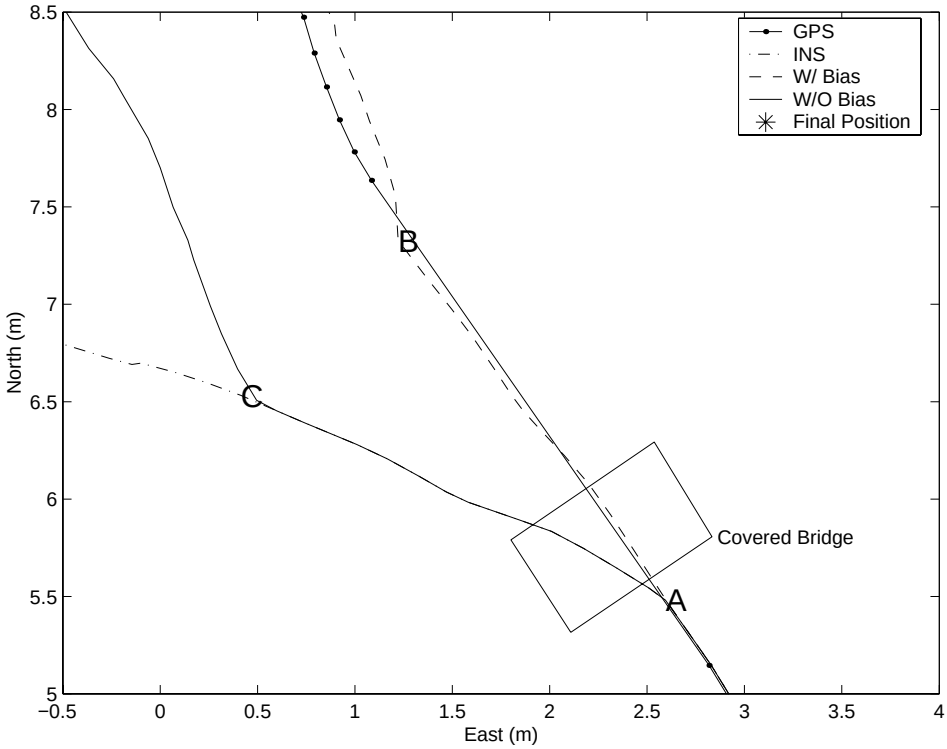

Figure 4-8: Area around GPS signal loss and reacquisition

do not provide any improvement of the accuracy of the INS devices. The dashed line indicates the results for the coupled measurement model formulated in section 2.2.2. Other information present shows the transmitter and receiver locations of the laser set-up indicated by T_1, T_2 and R, respectively. The final position of each filter is indicated by a circle at the end of the path. In order to determine the estimation error, the final actual position was marked relative to the start point on a paper grid aligned with the north-east reference frame.

Four areas of interest for the estimation are marked with A, B, C, and D. A close-up view of the area containing A-C is shown in figure 4-8. Estimation of all four filters begin from the origin and propagate to 'A' using the precise GPS Doppler measurements. At 'A', GPS measurements are blocked causing a discontinuity in the GPS only estimator until the signals were reacquired. The dead-reckoning straight line matches the path followed such that the time propagation is able to accurately move the position estimate forward until signals are available. Had the motion changed significantly in this region (i.e. accelerate or turn), the GPS-only estimator would be unable to accurately predict the position. The INS-only and the GPS/INS without modeled sensor bias filters immediately begin to diverge from the path due to sensor measurement error. As expected, the coupled GPS/INS filter with proper sensor measurement models is able to estimate the sensor error thus maintaining an accurate, continuous estimation of the vehicle state.

After the short delay due to GPS outage, the GPS/INS filters show another change in position results. 'B' indicates when the GPS/INS with bias models filter begins to use GPS measurements again for the estimation. Notice the minimal drift between this filter position estimate and the stand-alone GPS from 'A' to 'B'. The point 'C' indicates the same time as 'B' in which GPS measurements are used in the INS-only and GPS/INS w/o bias models filters. The INS-only version does not incorporate any GPS measurements after the first occlusion so the position error drift continues to grow without bound. On the other hand, the INS w/o bias models suddenly has precise velocity measurements which it can use to integrate for the position estimate. At this time, the INS w/ and w/o filters are shown to be parallel because they both use

the same GPS velocity measurements. The INS w/o filter, however, has a significant position error that cannot be corrected from velocity measurements alone. This error from the GPS/INS w/o filter demonstrates the added accuracy achieved by using simultaneous speed measurements to estimate the INS sensor errors.

Given the position errors caused by the GPS occlusion, the single point position fix is able to provide precise correction of the position estimation state. Figure 4-9 shows the area around 'D' in which the vehicles passes through the laser beam set. Note the significant discontinuity of the INS-only and GPS/INS w/o filters position update after the single point position measurement. This measurement is able to reset the drifting position error such that greater confidence in the state estimate is produced. The GPS/INS w/ bias filter appears smooth in this region but discrete positions for this figure are marked with ∘. The straight line connecting the area with no ∘'s indicates the single point position fix measurement adjusted the longitudinal vehicle position error, unlike the two dimensional adjustments made for the INS-only and INS w/o bias estimators. The GPS-only filter does not use the position measurement. The square on the GPS-only filter estimate denotes the time of breaking the second laser. After the reset, the two GPS/INS filters continue with almost the exact same position estimate again because they are using the same GPS velocity measurements. The INS-only filter again drifts rapidly away from the rest of the solutions indicating its inherent inaccuracy in state estimation. Note that the reset position is not immediately on the line connecting $\mathbf{T_2}$ and $\mathbf{R}$. A post was placed on the vehicle such that a single point would always break the laser beam rather than some unknown location on the truck. The offset between the post location and the vehicle reference causes this difference between the laser line and the reset position. Knowing the location of the post in the vehicle body frame and the rigid body orientation enables the correction to the vehicle position reset.

Figure 4-10 shows the final positions of all the filters. The position error was so large for the INS-only estimate that it is not within the axis limits. The two GPS/INS coupled filters are still parallel with the only difference caused by slightly different changes in the estimate due to the position updates when passing through

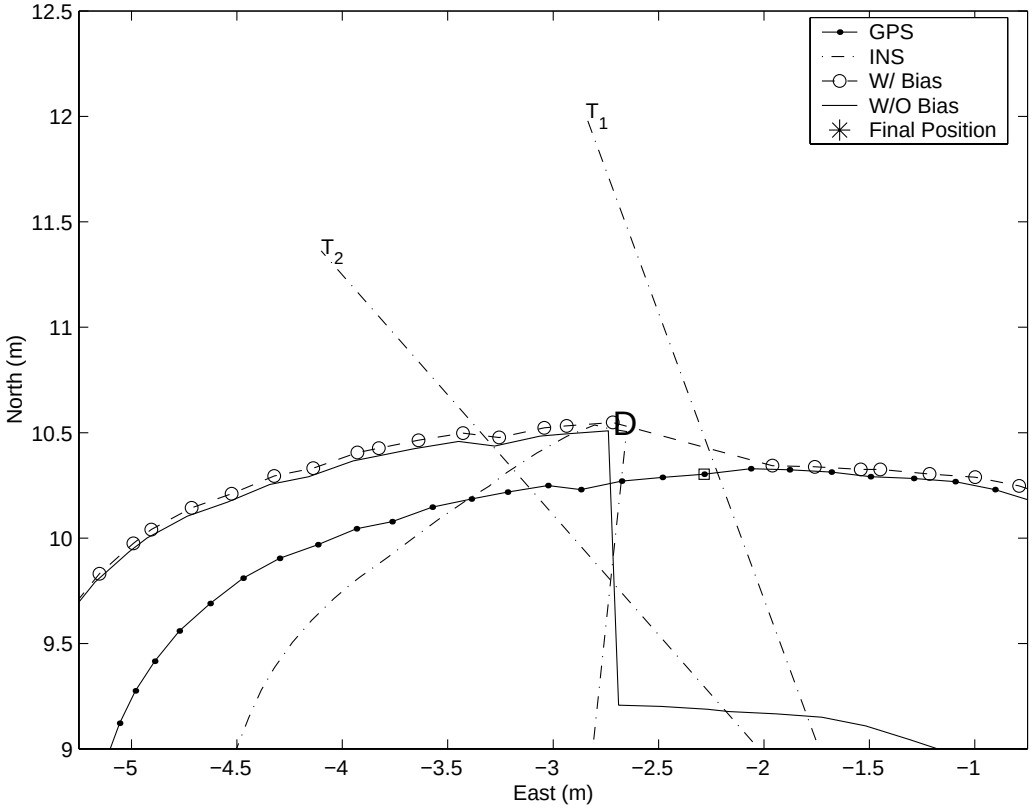

Figure 4-9: Close-up of area around single point position fix measurement

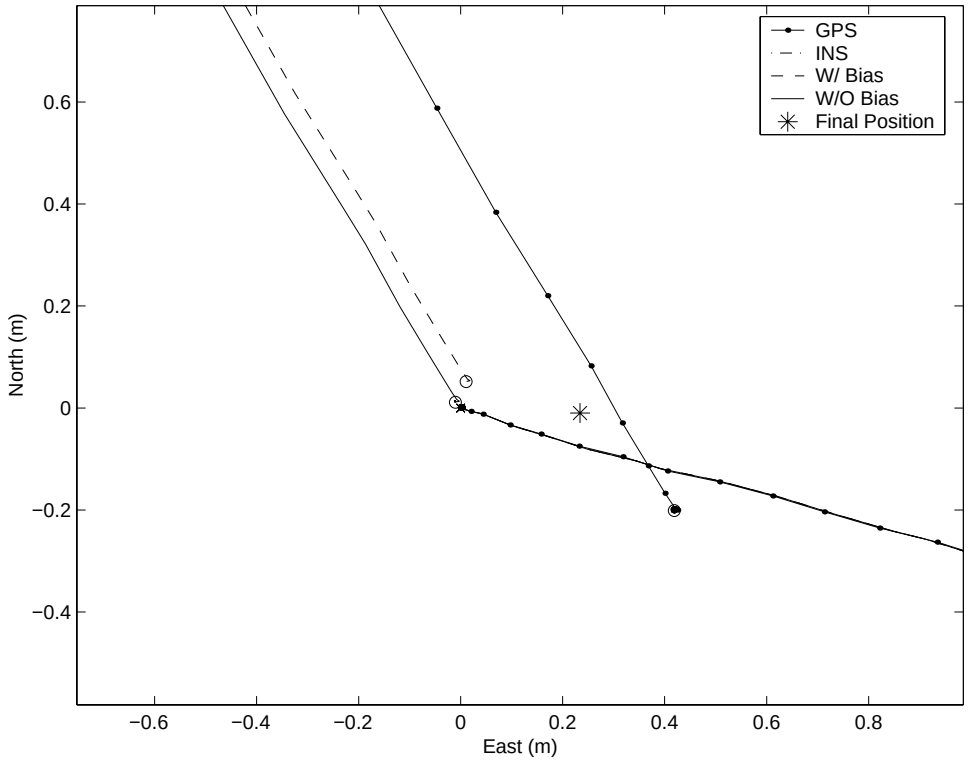

Figure 4-10: Area around start/finish position

the laser beam set. The control of the vehicle did not return the position exactly to the origin. The final actual position as measured on the paper grid indicated with an $*$ at position 1.0 cm south and 23 cm east. These values can be subtracted from the final results from the filters thereby indicating only the estimation error.

Results from three other experimental maneuvers are presented in Figures 4-11–4-13. The same areas of interest are identified indicating loss and reacquisition of GPS signals. The experimental run in figure 4-12 shows an additional loop near the finish point. The extra maneuver was required in order to return the truck to the position grid that was missed on the first pass, thereby enabling the final actual position to be recorded. Note that the estimation results presented in figures 4-12 and 4-13 are slightly different in that the GPS/INS estimator without sensor biases modeled does not show a sharp increase in position error drift. This would indicate that the sensor biases were small for this particular situation. This could be a result of magnetic disturbances changing during different experimental runs. The comparison of the estimator errors in the North-East directions for multiple experimental maneuvers is given in table 4.1. Comparison is made between estimators with and without the single point position fix. Significant improvement is noted for the GPS/INS w/o filter due to the large position error introduced during GPS outages. Without the reset, this error propagates to the final position. For the GPS/INS w/ bias filter, a smaller improvement is noticed. This is a result of good position estimation even during GPS outages. Overall, the table indicates the benefits of using the three pieces of the coupled sensor system.

While these results are not as accurate as continuous CDGPS, the Doppler integration method with backup inertial sensors and a single point position fix proves to be a more robust method for estimating accurate position comparison given an environment that has some occlusion to the NAVSTAR constellation.

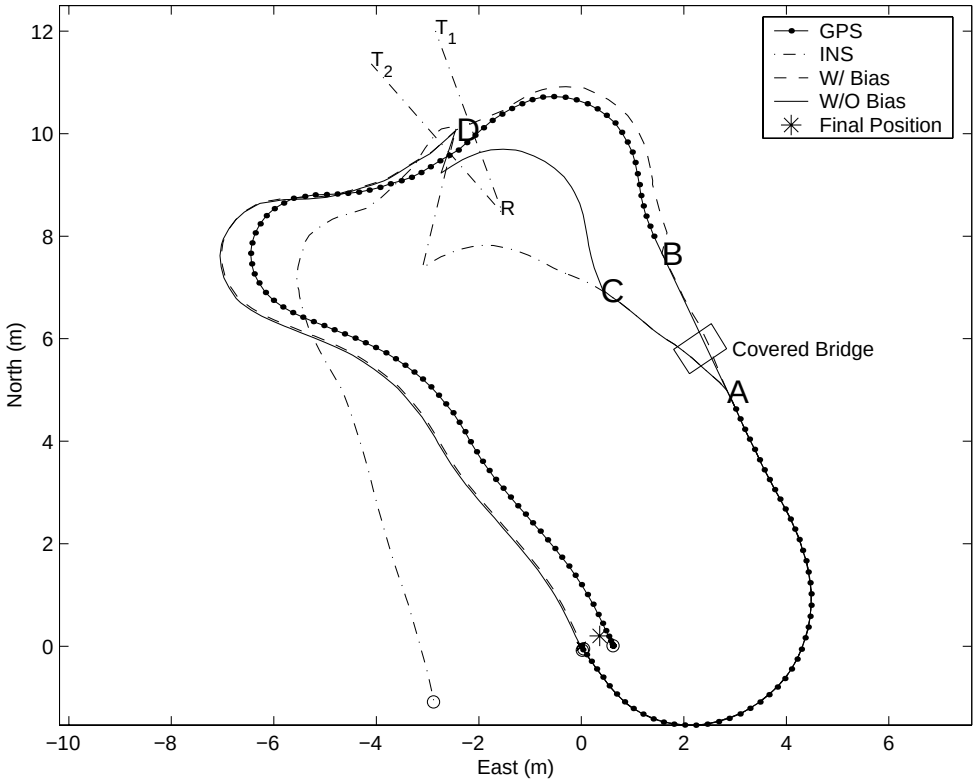

Figure 4-11: Position results of GPS and Coupled EKF - Run 35

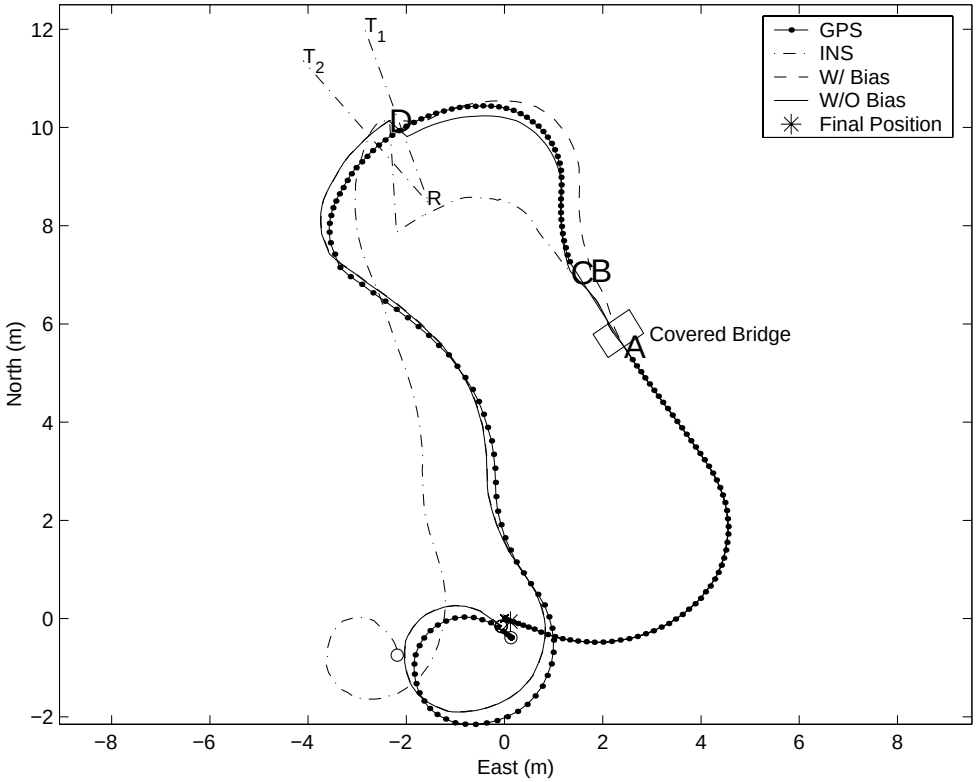

Figure 4-12: Position results of GPS and Coupled EKF - Run 37

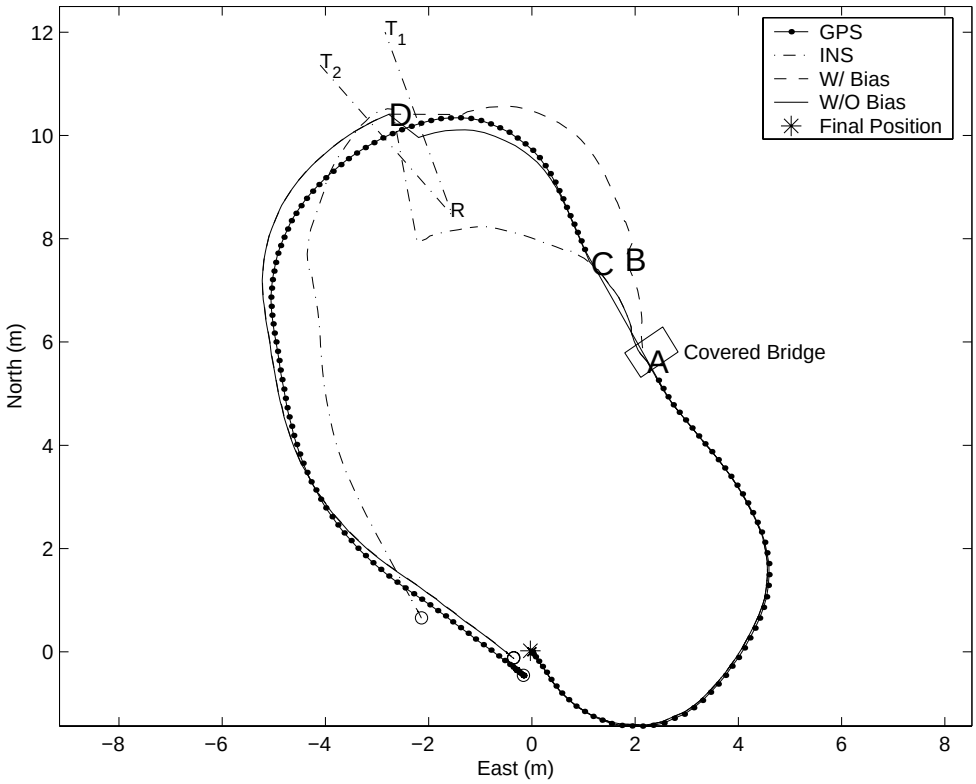

Figure 4-13: Position results of GPS and Coupled EKF - Run 39

Table 4.1: Estimation Error Results (m)

Estimator	GPS-INS w/ Bias		GPS-INS w/o Bias		GPS-INS w/ Bias		GPS-INS w/o Bias	
	Without Laser Reset				With Laser Reset			
Fig. No.	North	East	North	East	North	East	North	East
4-7	0.171	-0.287	1.310	0.440	-0.061	0.223	-0.021	0.224
4-11	-0.006	-0.467	1.214	0.760	0.253	0.316	0.281	0.340
4-12	0.212	-0.366	0.520	-0.015	0.095	0.182	0.102	0.190
4-13	0.242	-0.781	0.698	0.063	0.138	0.322	0.143	0.326

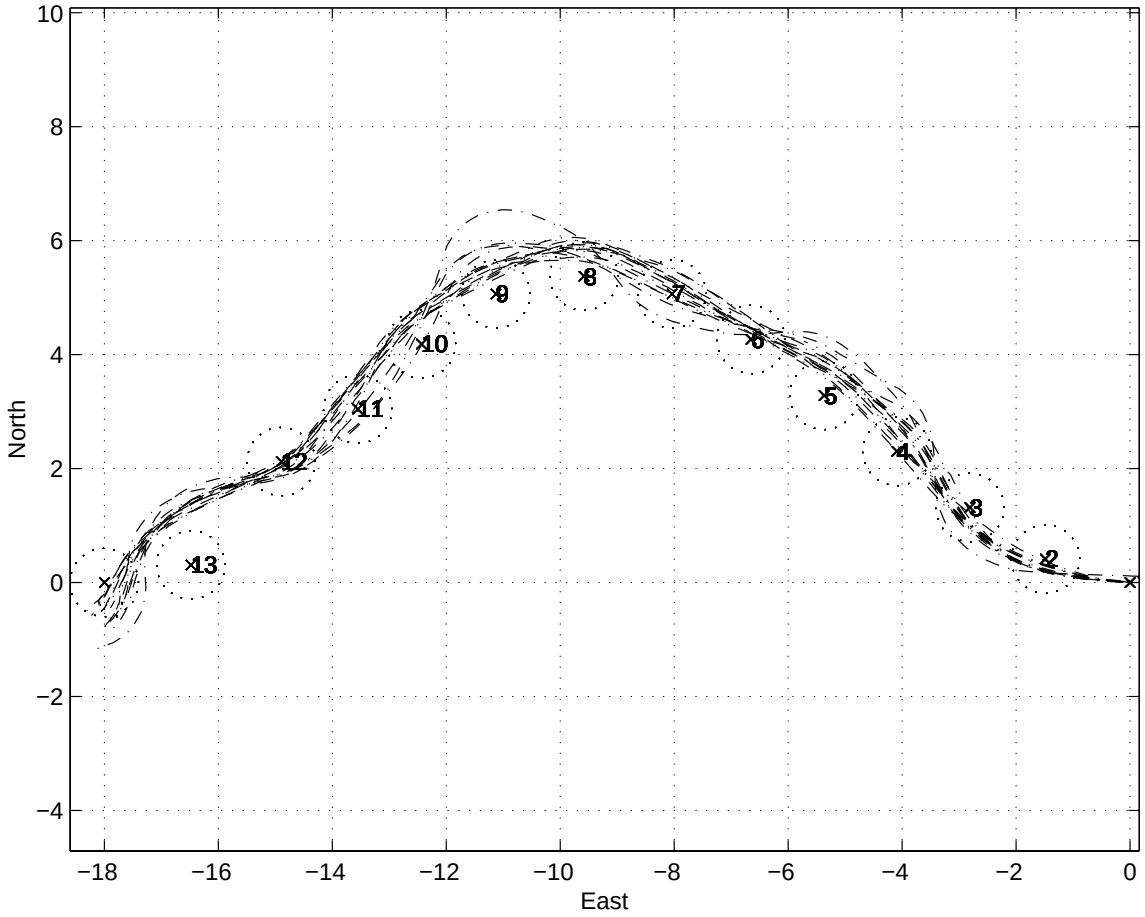

Figure 4-14: Multiple autonomous control runs

4.5 Control Results

4.5.1 Control of a Single Vehicle

For initial control algorithm verification, a plan was produced for a vehicle to travel from the origin to the location (-18,0). In order to verify control of non-straight paths, a curved plan was created between the origin and the target. Fifteen different runs of the vehicle starting at the same state with the same plan are shown in figure 4-14. The dash-dot lines indicate the position estimates provided from the real-time DGPS Doppler integration method. The path waypoints are indicated by $\times$ as well as the step number for the plan. The dotted circles around each waypoint show the decision areas to move the plan ahead one step. As expected some oscillation is seen around the nominal path due to overshoot of the heading and return to path control. Each

test resulted in the vehicle following the requested path.

Note that every test missed the second last waypoint (13) prior to entering the final target decision circle. During post-processing, a model mismatch was discovered that lead to a requested reduction of longitudinal speed in order to maneuver the sharp final turns. Since the low-level controller assumed a constant speed throughout, it became impossible for the vehicle to match the requested control to meet all the waypoint objectives. Note that despite this anomaly, the control algorithm was sufficiently robust to meet the final target, as it abandoned the infeasible waypoint and continued on with the plan.

The end point of each run was also recorded in order to determine the final position error of the estimator and controller. A paper grid was placed at the expected target and aligned with the N-E reference frame. The final estimation positions were overlaid with the final measured positions in figure 4-15. Note the large N-S bias observable between the estimated and measured positions. This was due to error in placing the final position grid. In order to place the position grid in the test area, a measurement was made from the origin to the desired location, (-18,0). The range was measured with a tape measure and angle set by a magnetic compass (after eliminating the declination between magnetic north and GPS frame north). Hence, the errors are unbiased in the east direction since they depended primarily on the precise range measurement. If the final measured positions are rotated by a single degree, the measurement accuracy of the compass device, the error bias in the N-S direction can almost be completely eliminated, as shown in figure 4-16. The results from the these tests demonstrate the accuracy of the estimation method. The primary reason for the minimal position error is due to continuous visibility to the GPS signals during the experiment.

Given that the error from the estimation can be eliminated from the final position, the actual control error was determined. As seen in figure 4-17, there is some small error in the E-W direction with most of the error bias coming from the N-S coordinate. This was due to the rolling stop after entering the final decision circle. Figure 4-14 shows that most of the paths entered the final decision circle heading in the south

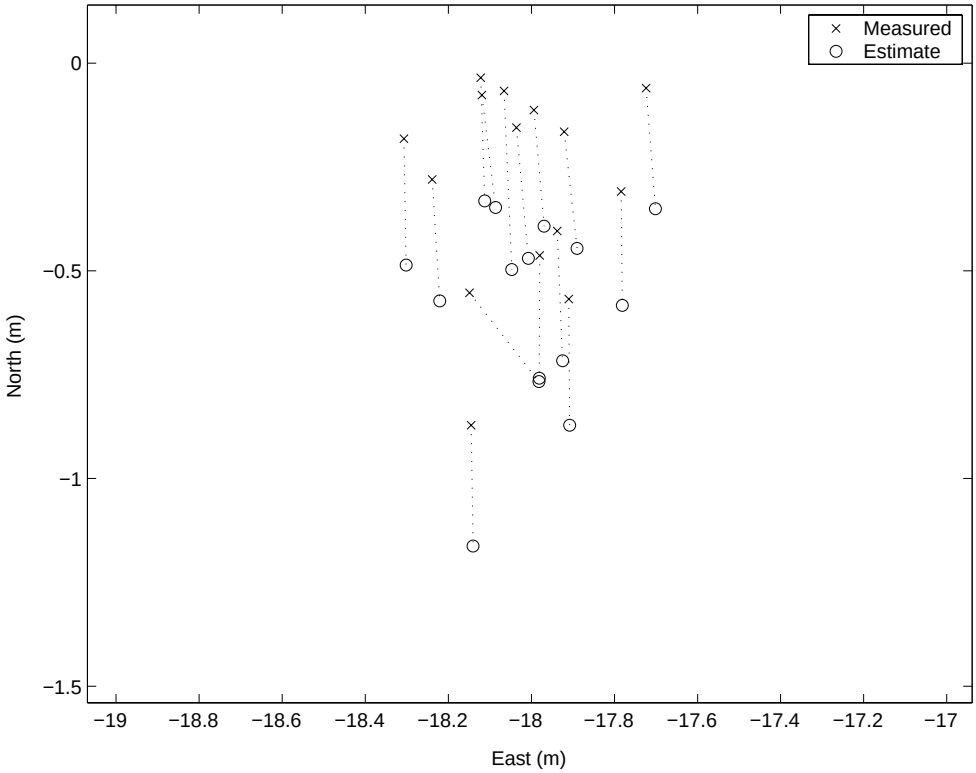

Figure 4-15: Final position of control experiments: ∘ indicates estimated value, × is the measured value for validation

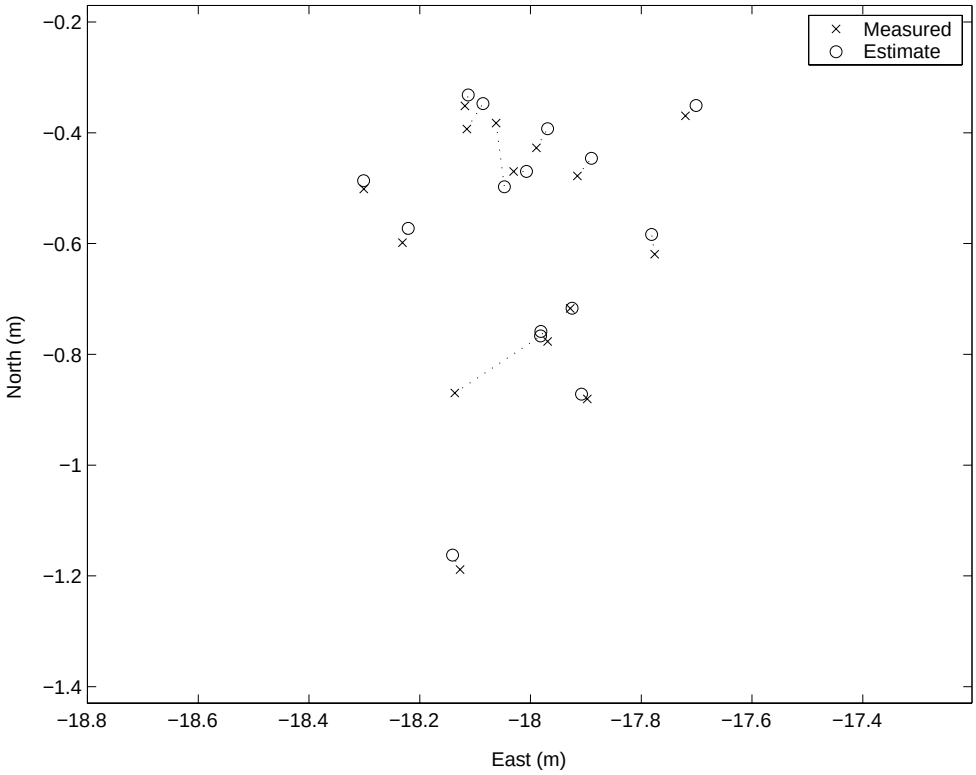

Figure 4-16: Final position of control experiment with rotated reference frame

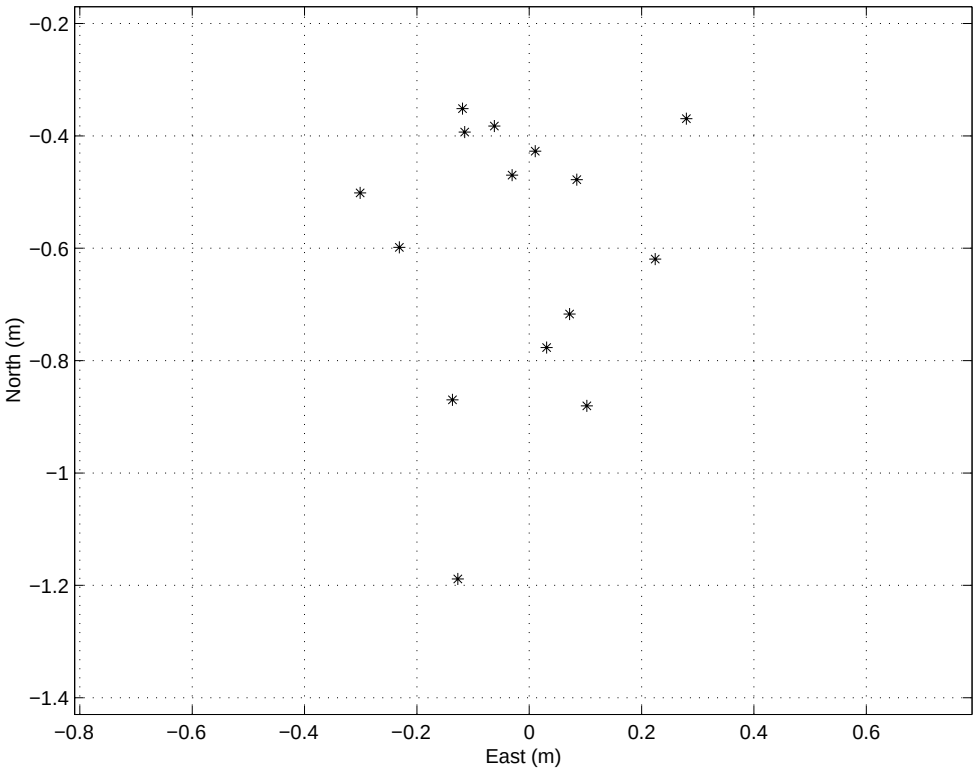

Figure 4-17: Control error of final position; Bias due to rolling stop of vehicle

direction. The controlled servo positions were immediately set to zero, but inertia and other lags result in the final control overshoot. Even with this simple stopping procedure, the control error was shown to be less than a meter for most cases.

4.5.2 Full Testbed Experiment

Given the ability to follow a nominal trajectory if the path waypoints are within the dynamic capability of the test vehicle, real-time planning algorithms can be tested. Most experiments attempt obstacle and collision avoidance for the experiment validation [45]. In the example shown in figure 4-18, two vehicles were started from known locations. State information for both was supplied to a planning computer using receding horizon control to quickly develop paths that would avoid the simulated obstacles as well as one another. The experimental result shows two vehicles trading places while maneuvering between obstacles. The solid rectangular boxes were the pre-surveyed obstacle locations. Due to discrete time enforcement of avoidance, the planner used enlarge models of the obstacles indicated by the dashed lines. The dots

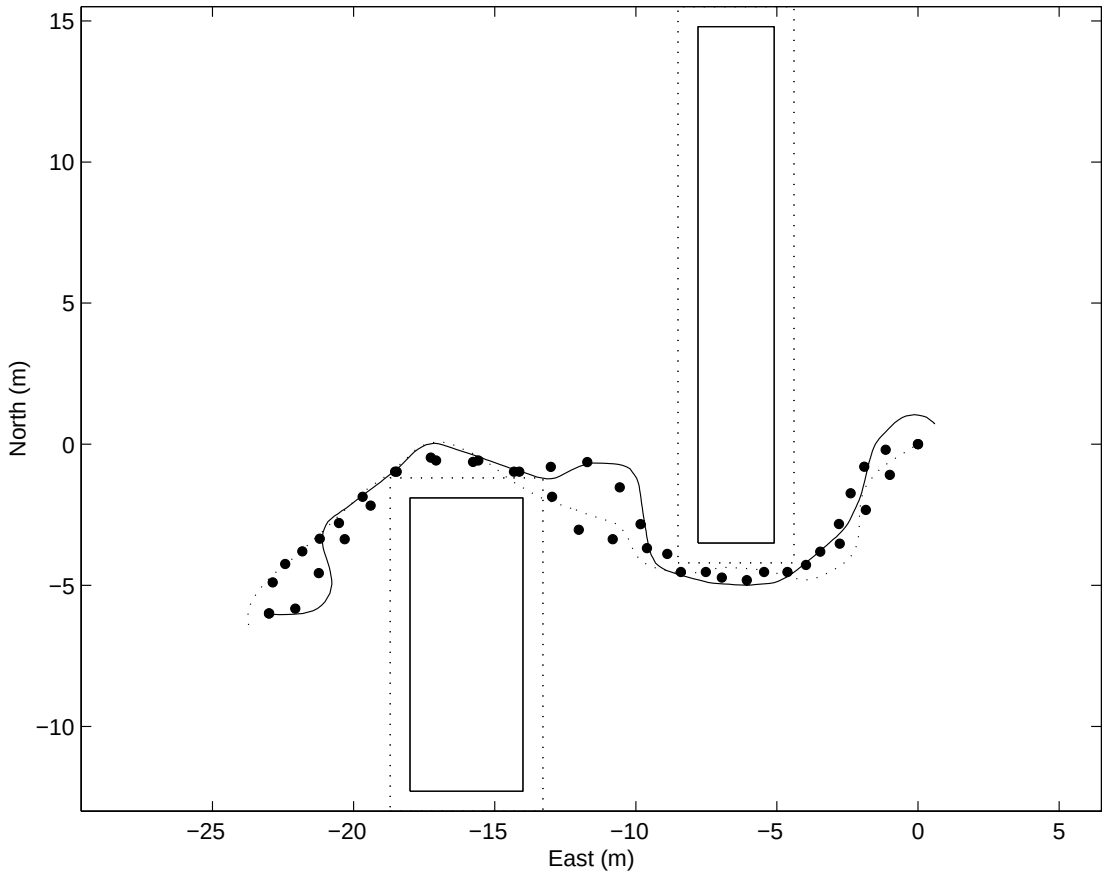

Figure 4-18: Two trucks trading places while avoiding obstacles and collision with one another

indicate the planned path with the solid line trajectory identifying the actual path traveled from west to east and the dashed line path going from east to west. The vehicles responded well to the provided plan and were able to meet their final position objective without encountering obstacles or one another.

Any planning algorithm can provide desired paths with appropriate state vector information to the testbed in order to conduct hardware-in-the-loop experiments. As an example, a dynamic planning algorithm was developed that only observed obstacles that were within a certain detection range of the vehicle position. The results of the experiment are shown in Figure 4-19. The real-time planner only attempts to avoid obstacles within a three meter radius of current position. To start, the planned path heads directly towards an obstacle, note the path following transient due to heading

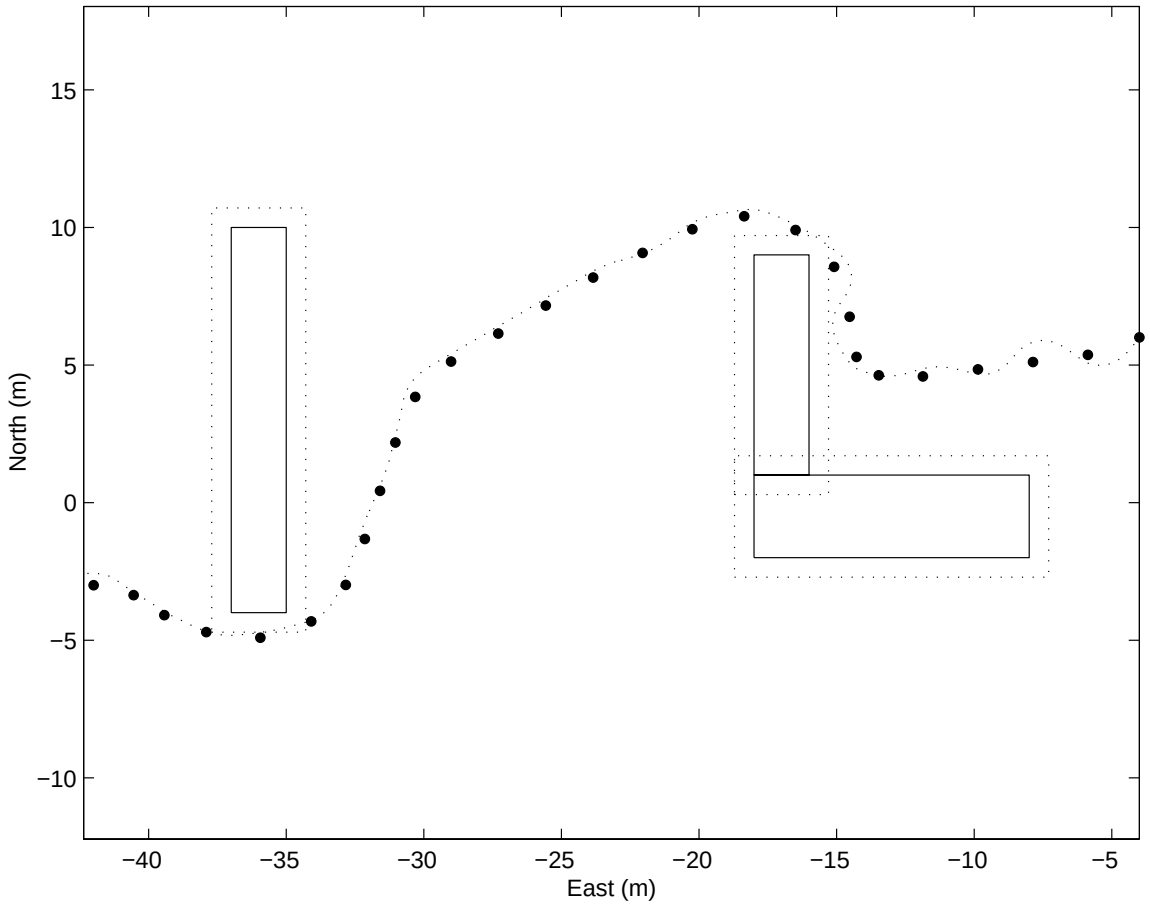

Figure 4-19: Test of dynamic planning algorithm that adjusts plan while maneuvering

mismatch. When the obstacle is within the detection horizon, the plan decides to change the path to avoid the obstruction. After turning around the top portion of the right obstacle, the plan continues on a straight line path to the target point $(-42, -3)$. An adjustment is later made around $(-28, 5)$ to avoid the second obstacle and still achieve the target objective. The experiment showed the testbed can be used to quickly perform hardware-in-the-loop tests of the dynamic planning algorithms.

4.6 Experimental Conclusions

All of the estimation and control algorithms developed in the preceding chapters of this thesis were tested and verified with hardware-in-the-loop experimentation. Results demonstrate that GPS signals and INS devices can be coupled to produce

accurate estimation (position error drift less than 2 mm/s) with a single position fix to periodically reset position error within a tolerance of 3 cm. The errors of estimation scale with the time, therefore the procedures used here for short-distance low-speed maneuvers are equally applicable to high-speed large-scale applications such as racecar applications to conduct precise comparison of multiple laps.

These results also indicate the utility of the developed multi-vehicle testbed. With the standardized interface, new algorithm developments in path planning can be verified with the fully operational testbed.

Chapter 5

Conclusions

5.1 New Estimation Method

This thesis demonstrates the sensor package and associated estimator developed in this research to provide an accurate estimation of vehicle state. During GPS signal tracking, good velocity and position estimation accuracy is achieved. Additionally, simultaneous measurements with INS devices enables estimation of sensor errors. Therefore, when GPS measurements are not available, the filter using only INS measurements and corrections is able to propagate a continuous accurate estimation of the state. Because the GPS and INS sensors all measure rates, a single point position fix is introduced to correct position error drift and/or initial position uncertainty. While the combined approach does not achieve the very high levels of accuracy available from CDGPS methods, the sensor package is able to maintain continuous estimation during signal loss and eliminates delay required for carrier-phase bias acquisition when signals are reacquired. Experimental results show a small drift rate of 1.0–3.0 mm/s when using the three elements of the sensor package.

5.2 Autonomous Testbed

Using the new algorithm, a complete hardware-in-the-loop testbed was developed to support future testing of path planning algorithms. The ground vehicles are controlled

by a base station computer via a two-way remote radio link. Low-level closed-loop control is performed on heading and speed. An outer-loop is used to control the vehicle such that it follows a supplied series of waypoints. The waypoints are provided to the control computer from a separate path planning computer via serial link. The programming and hardware allow for expansion of the numbers of vehicles that can be included in future experiments. Results indicate that if the provided path is within the dynamic capabilites of the testbed vehicles, the requested trajectory can be followed.

5.3 Future Work

5.3.1 Estimation

Work can be done to improve the overall accuracy of the estimation results. Most effort should focus on incorporating higher fidelity INS sensors thereby reducing the measurement noise. Improvements on Data-Acquisition techniques could also be incorporated to allow higher bandwidth measurement devices. Furthermore, improved design of the laser single point position fix hardware would reduce potential error introduced in the position measurement. As indicated in section 2.1.3, improvement in determining the spanned angle of the laser set-up will yield the most benefit to position measurement accuracy. Also, multiple position fix devices can be incorporated to correct position errors that drift during long elapsed time experiments.

5.3.2 Test Bed Improvements

Vehicle Expansion

Vehicle selection could be an additional parameter that is presented to a fleet planning algorithm. As designed, the current estimation/control method is expandable with vehicles matching the dynamic models presented. Work should be completed to add either specific capabilities to the vehicles already in use or potentially to include modes of transportation that are significantly different (i.e. planes and helicopters to

patrol the airspace; smaller vehicles for scout missions or larger vehicles for traversing particularly difficult terrain). This requires development of a new estimation filter to incorporate the differing dynamics and measurements, however all should easily fit into the communication architecture already developed.

Distributed of Computation and Architecture Reconfiguration

In order to construct a testbed completely autonomous from a base station control computer, work must be completed to adjust methods for the full fleet estimation and control. Onboard processors could be introduced to conduct estimation for individual vehicles within the fleet framework. Not only does this require hardware development but also some algorithmic changes that may be necessary depending upon the decentralizing nature of the measurements. Given the autonomous decision making capability that would be present in the decentralized estimation, dynamic network and architecture algorithms could be developed to optimize communication flow and structuring of subsections of the entire fleet.

Appendix A

Fabrication and Software Interface

A.1 Hardware Devices

This section presents the procurement of the major hardware components required for fabrication of the testbed. Table A.1 identifies the components necessary for complete autonomous vehicle construction with associated the manufacturer, vendor of purchase, part number, and cost. The same information is presented for all base

Table A.1: Testbed hardware list for ground vehicle

Item	Manufacturer	Vendor	P/N	Unit Price
Mammoth Dump Truck	Tamiya	Tower Hobbies	LXUU88	$399.99
Hi-Torque Servos	Hobbico	Tower Hobbies	LXPB37	$29.99
Smart Switch	B&B Electronics		232BSS4	$259.95
Radio Modem	Data-Linc Group		SRM6000	$887.50
SuperStar GPS Rxvr	CMC Electronics		220-604061-004 Option 3	$420.00
μ-controller	Motorola	New Micros	NMIX-0022 F68HC11	$130.00
Compass	Precision Navigation		Vector 2X	$69.99
Encoder	CUI Stack	Digikey	102-1002-ND	$39.85

station equipment in table A.2

Table A.2: Testbed hardware list for base station

Laptop	Toshiba	Best Buy	Satellite 1735	$1099.97
USB to 2 Serial Ports	Belkin	Belkin	F5U116	$179.95
USB to 1 Serial Port	Belkin	Belkin	F5U103	$59.95
Radio Modem	Data-Linc Group		SRM6000	$887.50
SuperStar GPS Rxvr	CMC Electronics		220-604061-004 Option 3	$420.00

A.2 Software Interface

The executable program "stargnd.exe" was created with the DJGPP compiler available at http://www.delorie.com/djgpp/. The program was able to communicate to the base station GPS receiver, each truck system via radio modem connection, and the planning computer on serial ports (COM1, COM2, COM3, COM4, respectively). To expand the number of serial ports on the laptop, the Belkin USB to serial adapter was used to create each serial port with enabled DOS-box option.

Tracking, control and estimation information were all displayed according to the current page display on the program. Table A.3 indicates the information shown when the current function key is depressed. Commands sent to the truck will change

Table A.3: Function keys to change display screen (follow each key hit with a spacebar hit)

F1	Help display showing function keys and commands
F2	Absolute navigation solution from the GPS receiver as well as current GPS week and time (update 1 Hz)
F3	Inertial measurements available from the truck compass, encoder and current servo settings for turn and speed control (update 10 Hz)
F4	GPS tracking display showing current satellites on 12 channels as well as SNR and LOS vectors (update rate according to rate of streaming measurements)
F5	Data messages received in hexidecimal (update 10 Hz)
F6	Real-time state estimation results (update 5 Hz nominal)
F7-9	Debug display screens for viewing other data
PgUp/PgDn	Scroll between base station and remote truck systems (F4-F6 displays)

data message rates and whether they are requested or streaming. A table of typical commands is shown in table A.4.

Table A.4: Commands for "stargnd.exe"; Press ESC key to obtain command prompt at bottom of display

LF FOO.M	Log file of current data with name beginning with FOO; Command again to stop logging data
SE 1	Start Estimation for truck number indicated
KE 2	Kill Estimation for truck number indicated
SG 1 N E	Set Goal to supply to planning computer
SP 1 N E	Set Position of the truck number state to desired north and east position
VC 3 speed	Velocity Control initiated with desired speed
KM	Kill Matlab communication link to planning computer
Other commands can be found and/or created in command.c of software files	

With fully charged batteries and the complete connections created per figure 4-2, the testbed should be operational for use with any planning algorithm or obstacle course.

Bibliography

[1] E. Olsen, *GPS Sensing for Formation Flying Vehicles*, Ph.D. thesis in the Dept. of Aeronautics and Astronautics, Stanford University, Dec. 1998.

[2] H. S. Cobb, *GPS Pseudolites: Theory, Design, and Applications*. Ph.D. thesis in the Dept. of Aeronautics and Astronautics, Stanford University, Dec. 1997.

[3] C. W. Park, *Precise Relative Navigation Using Augmented CDGPS*. Ph.D. thesis in the Dept. of Mechanical Engineering, Stanford University, June 2001.

[4] M. E. O'Connor, *Carrier-Phase Differential GPS for Automatic Control of Land Vehicles*. Ph.D. thesis in the Dept. of Aeronautics and Astronautics, Stanford University, Dec. 1997.

[5] C. .E. Cohen, *Attitude Determination Using GPS*. Ph.D. thesis in the Dept. of Aeronautics and Astronautics, Stanford University, Dec. 1992.

[6] D. Knight, "A New Method of Instantaneous Ambiguity Resolution," *Proceedings of the ION GPS*, Salt Lake City, UT, 1994, pp. 707–717.

[7] D. M. Bevly, J. C. Gerdes, C. Wilson, and G. Zhang, "The Use of GPS Based Velocity Measurements for Improved Vehicle State Estimation," *Proceedings of the American Control Conference*, Chicago, IL, 2000, pp. 2538-2542

[8] D. M. Bevly, R. Sheridan, and J. C. Gerdes, "Integrating INS Sensors with GPS Velocity Measurements of Continuous Estimation of Vehicle Sideslip and Tire Cornering Stiffness," *Proceedings of the American Control Conference*, Arlington, VA, June, 2001, pp. 25–30.

[9] R.P. Kornfeld, R. J. Hansman, J. J. Deyst, "Single Antenna GPS Based Aircraft Attitude Determination," *Proceedings of the ION Technical Meeting*, Long Beach, CA, Jan. 1998.

[10] D. Casanova, R. S. Sharp, and P. Symonds, "Construction of race circuit geometry from on-car measurements," *Proceedings of the Institution of Mechanical Engineers*, Vol 215, Part D, pp. 1033—1042.

[11] G. Wahba, "A Least-Squares Estimate of Spacecraft Attitude," *SIAM Review*, Vol. 7, No. 3, July, 1965, p. 409.

[12] D. G. Lawrence, *Aircraft Landing Using GPS.* Ph.D. thesis in the Dept of Aeronautics and Astronautics, Sept. 1996.

[13] R. B. Langley, "RTK GPS", *GPS World*, Vol. 9, No. 9, Sept. 1998, pp. 70–76.

[14] S. Han and C. Rizos, "Comparing GPS Ambiguity Resolution Techniques," *GPS World*, Vol. 8, No. 10, Oct. 1997, pp. 54–61.

[15] J. Meyer, *Coaching Tools for High-Performance Driving.* S. M. thesis in the Dept. of Mechanical Engineering, Massachusetts Institute of Technology, Feb. 2002.

[16] P. Hong, "GPS Basics", *Road & Track*, Sept. 2000, pp. 58.

[17] P. Ramanata, *Optimal Vehicle Path Generator Using Optimization Methods.* M. S. thesis in the Dept. of Mechanical Engineering, Virginia Polytechnic Institute, Apr. 1998.

[18] S. Kato and S. Tsugawa, "Lateral and Longitudinal Control Algorithms for Visual Platooning of Autonomous Vehicles," *Proceedings of the FISITA World Automotive Congress*, Seoul, Korea, June 2000.

[19] A. Hac and M. D. Simpson, "Estimation of vehicle Side Slip Angle and Yaw Rate," *Society of Automotive Engineers Technical Paper Series*, SAE 2000 World Congress, Detroit, MI, Mar. 2000.

[20] D. Wang, E. K. Tay, M. Zribi and E. K. Teoh, "A Lateral Control Scheme for a 4 Wheel Steering AGV," *Proceedings of IEEE Intelligent Vehicles Symposium 1998, IV98*, October 1998, Stuttgart, Germany, pp.107–112.

[21] K. Milnes and T. Ford, "Real-Time GPS FX: On-Screen Positioning of Racecars," *GPS World*, Vol. 12, No. 9, Sep. 2001, pp. 12–19.

[22] H. Z. Abidin, "On-the-Fly Ambiguity Resolution," *GPS World*, Vol. 5, No. 4, Apr. 1994, pp. 40–50.

[23] D. M. Bevly, A. Rekow and B. Parkinson, "Comparison of INS vs. Carrier-Phase DGPS for Attitude Determination in the Control of Off-Road Vehicles," *Navigation*, Vol. 47, No. 4, Winter, 2000-2001, pp. 257–266.

[24] W. T. Higgins, Jr., "A Comparison of Complementary and Kalman Filtering," *IEEE Transactions on Aerospace and Electronic Systems*, Vol. AES-11, No. 3, May 1975, pp. 321–325.

[25] D. Gebre-Egziabher, R. C. Hayward, and J. D. Powell, "A Low-Cost GPS/Inertial Attitude Heading Reference System (AHRS) for General Aviation Applications", *Position Location and Navigation Symposium, IEEE*, Jan. 1998, pp. 518–525.

[26] R. Smith, A. Frost, P. Roberts, "Gyroscopic Data Fusion via a Quaternion Based Complementary Filter", *SPIE*, Vol. 3067, pp. 148–159.

[27] M. E. Cannon, et al. "Development and Testing of an Integrated INS/GPS Cross-Linked System for Sub-Metre Positioning of a CF-188 Jet Fighter", *Canadian Aeronautics and Space Journal*, Vol. 46, No. 1, Mar. 2000, pp. 1–11.

[28] R. Harvey and M. E. Cannon, "A GPS-Based Integrated Sensor Approach to the Precision Positioning Problem", *Canadian Aeronautics and Space Journal*, Vol. 45, No. 3, Sep. 1999, pp. 297–306.

[29] A. Pascoal, "Navigation System Design Using Time-Varying Complementary Filters", *IEEE Transactions on Aerospace and Electronic Systems*, Vol. 36, No. 4, Oct. 2000, pp. 1099–1114.

[30] J. A. Farrell, T. D. Givargis and M. J. Barth, "Real-Time Differential Carrier Phase GPS-Aided INS", *IEEE Transactions on Control Systems Technology*, Vol. 8, No. 4, July, 2000, pp. 709–721.

[31] *SRM6000 Spread Spectrum Frequency Hopping Radio Modem, User's Manual*, Data-Linc Group, May, 2001.

[32] *User's Manual Superstar*, BAE Systems Canada, Inc., Apr. 2000.

[33] B. W. Parkinson and J. J. Spilker, Jr., Eds. *Global Positioning System: Theory and Applications, Vol. I*, Washington, DC: AIAA, 1996.

[34] B. Hofmann-Wellenhof, H. Lichtengger and J. Collins, *Global Position System: Theory and Practice*, Third ed. New York: Springer-Verlag Wien, 1994.

[35] GPS Joint Program Office. *ICD-GPS-200: GPS Interface Control Document*, Apr. 1993.

[36] R. G. Brown and P. Y. C. Hwang, *Introduction to Random Signals and Applied Kalman Filtering*, Third ed. New York: John Wiley and Sons, 1997.

[37] A. Gelb, ed. *Applied Optimal Estimation*, Cambridge, MA: The MIT Press, 1974.

[38] G. F. Franklin, J. D. Powell and A. Emami-Naeini, *Feedback Control of Dynamic Systems*, Third ed. Reading, MA: Addison-Wesly Publishing Company, 1994.

[39] J. Y. Wong, *Theory of Ground Vehicles*, 2nd ed., New York: J. Wiley, 1993.

[40] J. R. Ellis *Vehicle Handling Dynamics*, London: Mechanical Engineering Publications, 1994.

[41] F. Busse *Precise Formation State Estimation in Low Earth Orbit using GPS.* Ph.D. thesis in the Dept. of Aeronautics and Astronautics, Stanford University, Dec. 2002.

[42] J. P. How, N. A. Pohlman, and C. W. Park "GPS Estimation Algorithms for Precise Velocity, Slip, and Race-track Position Measurements", Accepted for publication at SAE 2002 Motorsports Conference, Indianapolis, IN, December 2-5,2002.

[43] P. Ferguson, et al., "Formation Flying Experiments on the Orion-Emerald Mission", AIAA Space 2001 Conference and Exposition, Albuquerque, NM, August 28-30, 2001.

[44] C. W. Park, J. P. How, and L. Capots "Sensing Technologies for Formation Flying Spacecraft in LEO Using CDGPS and an Inter-Spacecraft Communications System", *Proceedings of the ION GPS*, Salt Lake City, UT, 2000.

[45] J. Bellingham, *Coordination and Control of UAV Fleets using Mixed-Integer Linear Programming*, S. M. thesis in the Dept. of Aeronautics and Astronautics, Massachusetts Institute of Technology, Aug. 2002.

[46] P. Ferguson, *Decentralized Estimation Algorithms*, S. M. thesis in the Dept. of Aeronautics and Astronautics, Massachusetts Institute of Technology, Dec. 2002.

[47] *HC11: M68HC11 E Series*, Motorola, Inc., 1995.

[48] R. Gold, "Optimal Binary Sequences for Spread Spectrum Multiplexing", *IEEE Transactions on Information Theory*, October 1967, pp 619–621.

[49] Clinton, W., Presidential Press Release. Washington, DC, May 1, 2000.

[50] Kaplan, E. D., *Understanding GPS: principles and applications*, Boston: Artech House, 1996.

[51] J. P. How, "Notes for aircraft control course", Copyright, 1998.

[52] E. Prigge, "An Indoor Absolute Positioning System with No Line of Sight Restrictions", Ph. D. thesis in the Dept. of Aeronautics and Astronautics, Stanford University, Dec. 2002.

[53] T. Schouwenaars, B. DeMoor, E. Feron and J. How, "Mixed Integer Programming for Multi-Vehicle Path Planning," in the proceedings of the *European Control Conference,* European Union Control Association, Porto, Portugal, September, 2001, pp. 2603-2608.

[54] A. Richards, J. How, T. Schouwenaars and E. Feron, "Plume Avoidance Maneuver Planning Using Mixed Integer Linear Programming," in the proceedings of the *AIAA Guidance, Navigation, and Control Conference*, AIAA Paper 2001-4091, AIAA, Reston, VA, August 2001.

[55] J. S. Bellingham, A. G. Richards and J. P. How, "Receding Horizon Control of Autonomous Aerial Vehicles", presented at the *American Control Conference,* 2002.

[56] J. S. Bellingham, M. J. Tillerson, A. G. Richards, J. P. How, "Multi-Task Assignment and Path Planning for Cooperating UAVs," published in *"Cooperative Control: Models, Applications and Algorithms,"* Editors S. Butenko, R. Murphey, and P. Pardalos, Kluwer Academic Publishers, 2002.

[57] *Buffered Smart Switch, Instruction Manual*, B&B Electronics, April, 2000.